ELSEVIER

Coordination Chemistry Reviews
200–202 (2000) 443–485

COORDINATION CHEMISTRY REVIEWS

www.elsevier.com/locate/ccr

Understanding the dioxygen reaction chemistry of diiron proteins through synthetic modeling studies

J. Du Bois, Tadashi J. Mizoguchi, Stephen J. Lippard *

Department of Chemistry, Massachusetts Institute of Technology, Cambridge, MA 02139, USA

Received 14 October 1999; received in revised form 18 February 2000; accepted 23 February 2000

Contents

* Corresponding author. Tel.: +1-617-2531892; fax: +1-617-2588150.
E-mail address: lippard@lippard.mit.edu (S.J. Lippard).

PII: S0010-8545(00)00336-2

1. Introduction

The de novo construction of small-molecule, functional mimics of metalloenzymes offers unparalleled challenges to the chemist interested in ligand design, synthesis, coordination chemistry, molecular recognition, and catalysis. Nature has evolved elaborate polypeptide scaffolds to house metal cofactors using a relatively small assortment of coordinating groups [1,2]. The diversity in the structure and composition of these metal-containing active sites is reflected in the many different functions that they perform. In one class of metalloproteins, a dinuclear iron center serves as an essential component of the protein machinery required for dioxygen activation [3–7]. The structures of many of these diiron-containing macromolecules have been elucidated through extensive biochemical, spectroscopic, and crystallographic studies. Despite this knowledge, a detailed mechanistic understanding of how these proteins use two iron atoms to bind, reduce, and activate O_2 has yet to be delineated. The development of diiron complexes that reproduce both the structural and functional properties of the metallic cores of the proteins could aid significantly efforts towards this end. In addition, such compounds would hold great potential as homogenous oxidation catalysts or as reagents for dioxygen sensing and storage [8,9]. The biological relevance of and commercial interest in preparing diiron metalloprotein models has propelled intensive research in this area of bioinorganic chemistry [10].

The following review highlights recent investigations with small-molecule diiron systems focusing specifically on the synthesis and dioxygen reactivity of well-defined ferrous complexes. Numerous studies exist that describe the unique reactivities of iron(III) compounds with reducing agents and O_2 or with dioxygen equivalents such as hydrogen peroxide [11–13]. These efforts have added significantly to the overall understanding of the mechanisms of oxidation in biological systems. In particular, the recent synthesis and characterization of a mixed-valence Fe(III)/Fe(IV) adduct has provided valuable insight into both the structure and reactivity properties of highly oxidized iron centers [11]. The interested reader is referred to a number of informative reviews detailing this and other ferric model chemistry [14–16]. Our discussion focuses specifically on the reactions of diiron(II) centers with dioxygen. A brief survey of computational work, which has afforded fundamental insights to the mechanism of O_2 activation and substrate oxidation by diiron centers, is also included. We conclude by presenting our perspective on the important challenges that must be met in order to realize the ultimate goal of creating a functional model.

2. Background

A number of structural similarities occur among dioxygen-dependent, non-heme iron proteins [3,5–7,17]. These systems include hemerythrin (Hr), ribonucleotide reductase (RNR), methane monooxygenase (MMO), acyl–acyl carrier protein desaturase (acyl–ACP), toluene monooxygenase (TMO), alkene monooxygenase (AMO), and ω-alkane hydroxylase (AlkB). Most contain carboxylate-bridged diiron clusters within a four-helix bundle motif. The desire to understand the active-site details that promote and control the rich chemistry exhibited by these biomolecules continues to arouse the interests of many researchers. Synthetic chemists interested in understanding the principles underlying the chemistry of diiron proteins have been guided by structural and mechanistic information derived from direct investigations of the biological systems. The following section provides a brief description of each of the proteins listed above.

2.1. Hemerythrin

Hemerythrin is an oxygen-carrier protein found in marine invertebrates [18–20]. Unlike its mammalian counterparts, myoglobin and hemoglobin, Hr houses a non-heme diiron cluster in its active site. This center is buried within a four-helix bundle, which constitutes one subunit of a protein complex that is typically multimeric. Each dinuclear site contains two μ-1,3-carboxylate groups and a single oxo-atom bridge (Fig. 1) [21–24]. The rest of the coordination sphere around each iron atom comprises imidazole groups from five histidine residues. Diferrous and diferric forms of Hr have been characterized both spectroscopically and crystallographically [19,25,26]. The fully reduced deoxy state (deoxyHr) maintains one coordinatively saturated six-coordinate ferrous ion (Fe_1) and one five-coordinate center (Fe_2). At the diiron(II) oxidation level, the bridging oxygen atom is protonated. Binding and concomitant two-electron reduction of O_2 occurs at Fe_2,

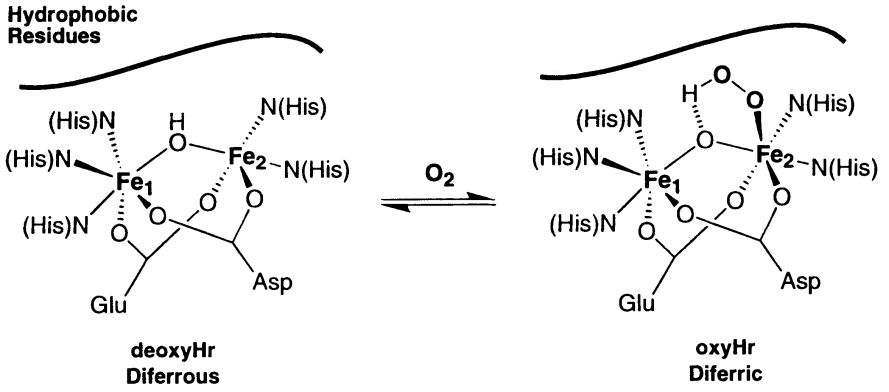

Fig. 1. Active site structures of deoxyHr and oxyHr.

affording a complex in which both iron centers are trivalent (oxyHr). X-ray crystal structures of oxyHr reveal that O_2 is bound as the hydroperoxide anion in a bent orientation that allows for hydrogen bonding to an oxo bridge [21]. The O–O distance between the terminal hydroperoxide oxygen atom and the oxo ligand is 2.8 Å, well within hydrogen bonding range. Resonance Raman (rR) spectroscopy confirms the assignment of a peroxide ligand in oxyHr with an observed ν_{O-O} stretching frequency of 844 cm^{-1} [27]. In addition, rR spectra taken in H_2O and D_2O show a 4 cm^{-1} shift to higher energy in the δ_s (Fe–O–Fe) vibrational mode when –OOH···O is replaced by –OOD···O [24]. This observation offers the most compelling evidence for the existence of a (hydroperoxide)–(μ-oxo) hydrogen bond (Fig. 1).

The mixed-valence Fe(II)/Fe(III) form of Hr (semimetHr) has also been investigated [28,29]. It is unstable towards spontaneous disproportionation, reflecting a predisposition of the diiron core to undergo two-electron redox steps. This property has significant ramifications; when dioxygen reacts with deoxyHr, the ferric hydroperoxide is formed directly. The stability of the hydroperoxide with respect to loss of superoxide ($HO_2^{\bullet}$) or superoxide anion ($O_2^{\bullet -}$) and concomitant generation of semimetHr wards against the deleterious production of highly reactive radical species. As will become apparent, other diiron metalloenzymes are also programmed inherently as two-electron reducing agents.

2.2. Ribonucleotide reductase

Ribonucleotide reductases (RNRs) catalyze the conversion of nucleotides to deoxynucleotides in what constitutes the rate-determining step in DNA biosynthesis [30–32]. Four classes of the RNRs have been identified and are categorized by their unusual cofactors [33]. We restrict the following discussion to the class I reductase isolated from *Escherichia coli*. Recently, the X-ray structure of a related class I RNR from *Salmonella typhimurium* has been determined [34].

Class I RNRs consist of a homodimer of two subunits, R1 and R2. Within each R2 domain there exists a dinuclear iron cluster positioned adjacent to a tyrosine residue (Tyr-122) [35]. Several forms of the R2 protein have been characterized structurally and spectroscopically. The active form $R2_{act}$ includes a diferric iron core and a stable tyrosyl radical (Tyr-122$^{\bullet}$). Tyrosine-122$^{\bullet}$ may be reduced selectively to furnish an inactive form of the protein, $R2_{met}$. The fully reduced state $R2_{red}$ is generated either upon anaerobic addition of Fe^{2+} salts to the apoprotein or upon treatment of $R2_{act}$ with various reducing agents. Exposure of $R2_{red}$ to O_2 and extra reducing equivalents results in the formation of Tyr-122$^{\bullet}$ and the diferric cluster [36–38]. Tyrosine-122$^{\bullet}$ functions to initiate multiple turnover, one-electron oxidations of a remote cysteine in the R1 subunit. The iron center is employed specifically for the activation of the Tyr-122 radical and does not play a role in the subsequent catalytic chemistry that leads to nucleotide reduction.

The structure of the dinuclear core in R2 has several features that distinguish it from Hr, but which are similar to those found in other dinuclear iron proteins. Two imidazoles and four carboxylates comprise the endogenous ligand set from amino

acid side chains (Fig. 2). In the X-ray structure of $R2_{red}$, two carboxylates bridge two four-coordinate ferrous centers [39]. The coordination sphere about each metal ion is completed with a single monodentate carboxylate and one imidazole donor. Oxidation of $R2_{red}$ results in a 'carboxylate shift' of one of the bridging carboxylates. A water molecule occupies a site on Fe_1 left vacant by the repositioned carboxylate. In addition, an oxo group, together with a single carboxylate, now links the two six-coordinate ferric centers. Other changes occur exclusively at Fe_2, which include the addition of a water molecule to its coordination sphere. The Fe···Fe separation in $R2_{red}$ contracts from 3.8 to 3.4 Å upon oxidation of the diiron core. Rather dramatic structural differences in the reduced versus oxidized state of the metallocofactor in R2 are also observed for MMO and Δ^9D, and are particularly relevant with respect to the design of functional model systems (vide infra).

2.3. Methane monooxygenase

Methanotrophic bacteria employ a multicomponent protein to catalyze the selective oxidation of methane to methanol, an essential step in the metabolic cycle of these organisms [3,5,40–42]. The soluble form of this enzyme, sMMO, can be expressed under conditions in which the growth medium is deficient in copper [43–45]. Studies on sMMO have been performed primarily with protein isolated from two bacterial strains, *Methylococcus capsulatus* (Bath) and *Methylosinus trichosporium* OB3b. Although there are specific differences between the sMMO produced by these two organisms, their active-site structures share many common features, and their oxidation mechanisms are believed to be analogous. For the purpose of this review, we shall discuss structural and mechanistic work reported for the *M. capsulatus* (Bath) system.

Soluble methane monooxygenase is composed of three constituent proteins: (1) a hydroxylase that houses two dinuclear iron centers; (2) a reductase (MMOR), which funnels reducing equivalents from NADH to the active site; and (3) a coupling protein (MMOB) needed to modulate the reactivity between hydroxylase, reductase, and substrates [46–49]. The hydroxylase (MMOH) is dimeric, having a $\alpha_2\beta_2\gamma_2$ composition and a metallocofactor located in each α subunit [50,51]. The coordination environment of these diiron sites in MMOH is quite similar to that found in class I RNRs. An X-ray crystal structure of the reduced form of MMOH shows two carboxylates linking two five-coordinate ferrous ions (Fig. 3). Two additional carboxylates, two imidazoles, and a single water molecule complete the coordination spheres about both irons. In contrast to RNR, one of the bridging carboxylates is positioned in a 1,1-coordination mode and is chelated to one Fe^{2+} center. The same carboxylate shifts to a terminal, monodentate geometry upon oxidation to the diferric core. The structure of the diiron(III) complex in $MMOH_{ox}$ also shows two single-atom bridging groups, assigned as water and/or hydroxide ions, depending upon crystallization conditions [52].

More distinct differences in the active sites of MMOH and R2 become apparent in the second shell of the diiron coordination sphere. The presence of a cysteine (Cys-151) in the space occupied by Try-122 in R2 suggests a possible role for the

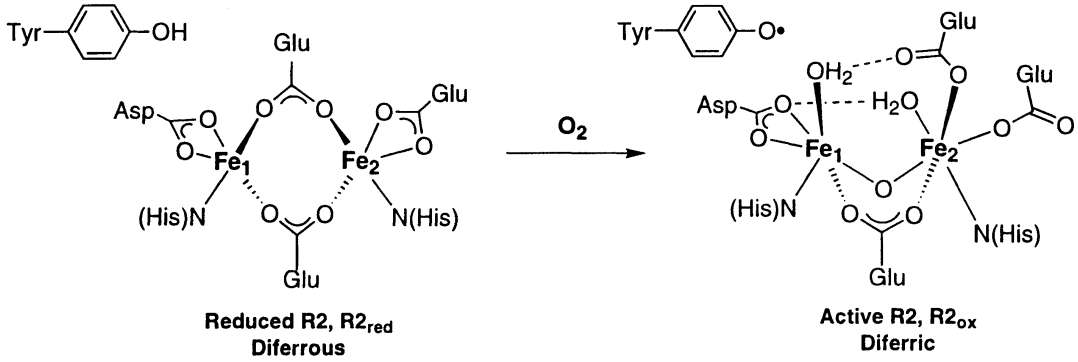

Fig. 2. Structure of diiron cofactor in ribonucleotide reductase in its reduced ($R2_{red}$) and oxidized ($R2_{ox}$) forms.

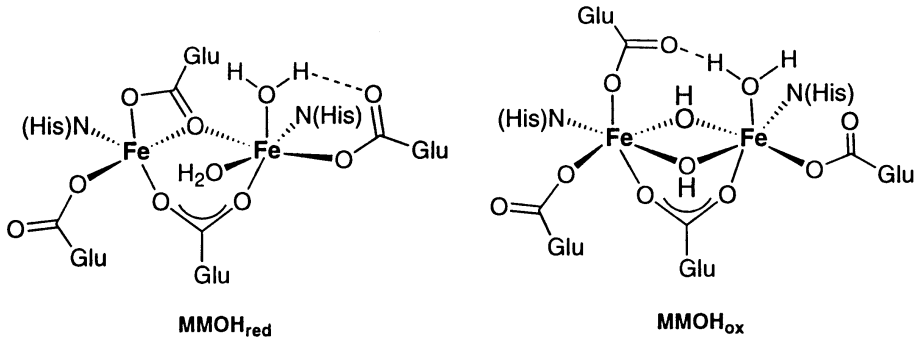

Fig. 3. Dinuclear iron center in reduced ($MMOH_{red}$) and oxidized ($MMOH_{ox}$) methane monooxygenase.

sulfhydryl moiety as a one-electron source and/or as a proton donor [3,53]. A threonine (Thr-213) situated adjacent to the iron cluster may also participate in the oxidation reaction by functioning as a proton source. Such a role for Thr-213 would be mechanistically analogous to that of Thr-302 in the related heme oxygenase, cytochrome P450 Δ2B4 [54]. Other amino acids residues of note are Asp-143 and Asp-242, each of which hydrogen bond to the ε-NH of an imidazole ligand [55]. Only one such hydrogen-bonding interaction is found in the RNR active site [4,56,57]. These aspartates may serve to alter the donating strength of the imidazole groups throughout the reaction cycle of the enzyme. In the limit that the ε-NH of the imidazole is deprotonated, the resultant imidazolate anion would serve as a strong σ-donor, possibly needed to stabilize high-valent iron intermediates.

2.4. Acyl–acyl carrier protein desaturase

Fatty acid desaturases catalyze the regio- and stereospecific insertion of a *cis* double bond into the alkyl chain of an acyl carrier protein-linked fatty acid [58–60]. Among these enzymes, the best characterized is the soluble stearoyl–acyl carrier protein Δ^9-desaturase (Δ^9D) isolated from castor seeds. This protein oxidizes the 9 and 10 positions of stearoyl-ACP to generate oleoyl-ACP in a dioxygen- and NADPH-dependent process [61–64]. Δ^9-Desaturase, like R2 and MMOH, is a homodimer with each subunit containing one dinuclear iron cluster. Only the reduced form of this protein has been characterized crystallographically [62]. The active-site structure shows two Fe^{2+} ions bound in a highly symmetric environment, reminiscent of the dinuclear core in R2 (Fig. 4). Two μ-1,3-bridging glutamates span two iron centers separated by a 4.2 Å distance. The diiron(III) form of Δ^9D has been investigated extensively by spectroscopic methods [63]. Results from these studies provide compelling evidence for the presence of a single μ-oxo ligand. Presently, this diferric cluster is believed to be structurally analogous to the diiron cofactor in $R2_{met}$.

In the absence of substrate, the reaction of the diferrous form of Δ^9D with O_2 induces a slow conversion to the diferric state [63,67,68]. This property is in distinct

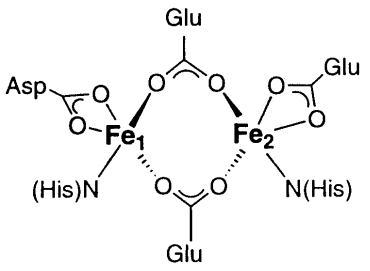

Fig. 4. X-ray crystal structure of the fully reduced stearoyl-ACP Δ^9 desaturase (Δ^9D).

contrast to the reactivity of $R2_{red}$, which is oxidized at the same rate with or without Tyr-122 present [69]. Similarly, the addition of methane increases only modestly the rate of $MMOH_{red}$ oxidation [5]. Recent circular dichroism (CD) and magnetic circular dichroism (MCD) studies show that the binding of stearoyl–ACP to Δ^9D causes a significant change in the metal ion coordination geometries [66]. These studies and the X-ray structure of reduced Δ^9D establish that both iron atoms of the cluster have nearly equivalent five-coordinate, distorted square pyramidal configurations. Spectral changes upon substrate binding indicate that one of these irons becomes four-coordinate while the other twists to trigonal bipyramidal geometry. The availability of an open coordination position on the four-coordinate center correlates nicely with the observed enhancement of dioxygen reactivity in the presence of stearoyl–ACP.

2.5. Toluene monooxygenase

A collection of soluble diiron enzymes known as toluene monooxygenases catalyzes the position-specific arene hydroxylation of toluene [5,7,70,71]. The best characterized among this group is toluene 4-monooxygenase (T4MO), a protein isolated from *Pseudomonas mendocina* KR1 that effects the regiospecific hydroxylation of toluene to *p*-cresol [72,73]. This four-component complex includes a reductase, a Rieske-type ferredoxin, a coupling protein, and a terminal hydroxylase. Analogous to MMO, the hydroxylase protein of T4MO is multimeric, having a $\alpha_2\beta_2\gamma_2$ subunit composition [6,73]. Each protomer contains a dinuclear iron site having the same Glu/Asp-X-X-His consensus sequence that provides the protein-derived ligands for the diiron clusters in MMOH, R2, and Δ^9D. Mössbauer and electron paramagnetic resonance (EPR) measurements show that the diferric resting state of the hydroxylase contains a hydroxo bridge, as in $MMOH_{ox}$. No X-ray crystal structure of an oxidized or reduced form of a TMO has been reported to date. An expression system for the active enzyme in *E. coli* has made possible the use of site-directed mutagenesis to probe the influence of specific amino acid

residues on the catalytic oxidation mechanism [70]. Such investigations have demonstrated that mutants of the wild type hydroxylase are capable of oxidizing both arene and benzylic C–H bonds of methylated benzene substrates (e.g. toluene, *o*- and *p*-xylene). These results suggest that the regiospecificity observed for *para*-hydroxylation by T4MO is the result of substrate orientation by the hydrophobic surface of the active-site cavity rather than an inherent mechanistic barrier to oxidation of aliphatic hydrocarbons. It is interesting to note, however, that methane and other small, saturated alkanes do not react with T4MO.

2.6. Alkene monooxygenase

Alkene monooxygenases (AMO) isolated from many different strains of bacteria function as multicomponent proteins for the stereoselective epoxidation of alkene hydrocarbons [74–76]. A recently characterized AMO from *Xanthobacter* strain Py2 is quite similar to T4MO, consisting of a two-part electron-transfer component (reductase and Rieske-type ferredoxin), an oxygenase, and a small effector protein [77,78]. The presence of a non-heme, dinuclear iron active site in each $\alpha\beta\gamma$ unit of the hydroxylase is likely, based on peptide sequence homology with other diiron proteins and preliminary spectroscopic measurements. Alkene monooxygenase systems from other bacterial sources contain three component proteins, and thus closely resemble sMMO [75,79]. In general, AMO systems have a more restricted substrate profile than other monooxygenases and are incapable of catalyzing the hydroxylation of saturated hydrocarbons. A rationalization for the observed reactivity differences between such seemingly similar enzymes has not yet evolved.

2.7. ω-Alkane hydroxylase

The integral-membrane protein alkane ω-hydroxylase (AlkB) is a requisite constituent of a ternary enzyme complex that performs the hydroxylation of unactivated aliphatic methyl groups [80,81]. The expression of catalytically active AlkB from *Pseudomonas oleovorans* in *E. coli* has been achieved, but little is presently known about the structure of the non-heme iron site(s) in this system. The ferrous form of AlkB appears to react with dioxygen only in the presence of substrate, behavior reminiscent of Δ^9D. Unlike Δ^9D and other carboxylate-based diiron proteins, however, AlkB contains an eight-histidine sequence motif common to integral-membrane hydroxylases and desaturases [82,83]. It has been proposed that these essential histidine residues serve as ligands in the catalytic domain of this protein family. Thus, AlkB may be representative of a distinct class of diiron enzymes that employ a nitrogen-rich metal coordination environment for O_2 activation and hydrocarbon oxidation. The potential for oxygenase activity from an imidazole-rich system is particularly intriguing given the function of hemerythrin for oxygen storage and transport, to date the only well-characterized polyimidazole diiron protein [1,4,7].

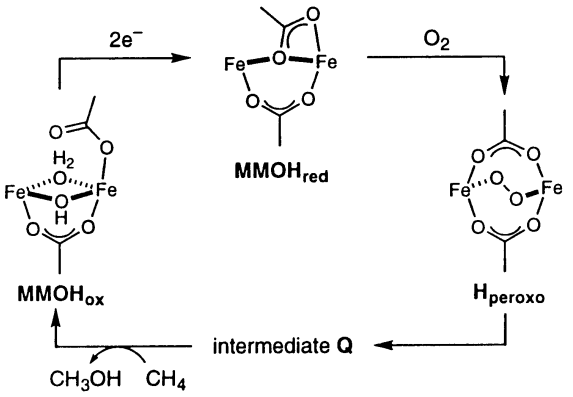

Scheme 1.

2.8. Mechanistic proposals

Similarities between the active-site structures of R2, MMOH, Δ^9D, T4MO, and AMO raise prospects that there exists a universal mechanism by which these systems operate. For the purpose of the following discussion, we shall use sMMO as a case study to present a mechanistic model for the reaction of dioxygen, reduced protein, and substrate. Where relevant, related findings with other diiron enzymes will be highlighted.

The reaction of $MMOH_{red}$ with O_2 has been investigated by stopped-flow optical spectroscopy [84–87]. These studies established the first-observable intermediate as a diferric peroxide, H_{peroxo} (Scheme 1). The optical spectrum of this species displays two characteristic bands with $\lambda_{max} \sim 420$ and ~ 725 nm, comparable to data recorded on small-molecule $Fe_2(O_2)$ analogs (vide infra) [88,89]. The assignment of H_{peroxo} as a diferric derivative was corroborated using Mössbauer spectroscopy [90]. Although the isomer shift ($\delta = 0.66$ mm s^{-1}) and quadrupole splitting ($\Delta E_Q = 1.55$ mm s^{-1}) are unusual for high spin iron, similar values have been reported for a diiron(III) μ-1,2-peroxide model complex [89]. The lack of an EPR signal due to antiferromagnetic spin exchange offers additional support for the presence of an O_2^{2-} ligand that bridges both ferric ions [91]. Moreover, a single quadrupole doublet in the Mössbauer spectrum of H_{peroxo} suggests that the O–O moiety is bound symmetrically between the two metal centers.

The mechanism of dioxygen activation has been similarly followed in site-directed mutant proteins of R2 [39,92,93]. Results from these studies demonstrated that a peroxo adduct is formed as the first observable intermediate. Oxygenation of the reduced Asp84Glu mutant R2 protein results in a relatively long-lived species ($t_{1/2} \sim 0.75$ s at 5°C) that shows a broad optical absorbance centered at 700 nm [94]. Mössbauer analysis revealed this species to be diamagnetic with $\delta = 0.63$ mm s^{-1} and $\Delta E_Q = 1.58$ mm s^{-1}. More definitive proof of an $Fe_2(O_2)$ adduct was obtained from rR spectroscopy on a double mutant of R2 [95]. An isotopically sensitive

vibration for ν(O–O) at 870 cm^{-1} and two Fe–O_2 bands at 458 and 499 cm^{-1} correspond closely to rR data reported for bridging peroxodiferric models. Furthermore, spectra collected on this intermediate prepared with mixed-isotope $^{16}O^{18}O$ indicate that the O_2^{2-} unit is symmetrically coordinated, most likely in a μ-1,2 mode.

Similar rR and optical spectroscopic data have been accumulated from studies with Δ^9D [63,65,67]. Addition of O_2 to the complex of stearoyl–ACP and fully reduced Δ^9D results in the formation of a metastable intermediate with a broad absorption maximum at 700 nm. This species shows rR vibrational features that correspond to ν(Fe–O_2) at 442 and 490 cm^{-1} and ν(O–O) at 898 cm^{-1}. A relatively high ν(O–O) value coupled with the observation of two Fe–O_2 modes suggests strongly a 1,2-bridging coordination geometry for the peroxide unit.

Insight into the electronic properties and reactivity behavior of μ-1,2-(peroxo)diferric adducts has been gained through detailed vibrational and optical spectroscopic studies on a small-molecule complex derived from tris(pyrazolyl)borate, $[Fe_2(O_2)(OBz)_2\{HB(pz')_3\}_2]$ (Fig. 5) [96]. An X-ray crystal structure of a related compound $[Fe_2(O_2)(O_2CBn)_2\{HB(pz')_3\}_2]$, in which the benzoate ligands were replaced by phenylacetate groups, reveals an Fe–O–O–Fe dihedral angle of 52.9° [89]. The gauche orientation of the two irons in $[Fe_2(O_2)(O_2CBn)_2\{HB(pz')_3\}_2]$ is unique in $Fe_2(O_2)$ model systems. The rR ν(O–O) stretching frequency of $\sim$875 cm^{-1} and unusual Mössbauer parameters ($\delta = 0.66$ mm s^{-1}, $\Delta E_Q = 1.40$ mm s^{-1}) correlate almost precisely with data obtained for H_{peroxo}, an R2 mutant, and Δ^9D. Thus, it has been concluded that the reaction of O_2 with the ferrous form of these proteins generates a 1,2-peroxide with an acute Fe–O–O–Fe dihedral [89]. In this geometry, coordination of the O_2^{2-} unit to the ferric centers is dominated by strong π-bonding interactions. As a result, there exists significant mechanical coupling between the Fe–O and O–O stretching motions, giving rise to the large observed ν(O–O) frequencies [96]. Interestingly, π back-bonding from the Fe(III) d-manifold into the O–O σ*orbital, as occurs in dicopper(II) μ–η^2:η^2-peroxides, does not appear to be energetically favorable. One conclusion from these spectroscopic and theoretical studies is that the bridging peroxide has basic/nucleophilic character. We shall return to these ideas in greater detail later in the review.

Iron(IV) intermediates have been implicated as the active oxidants in R2, sMMO, and other non-heme iron oxygenases [3,5,6,97]. With the use of Mössbauer, EPR,

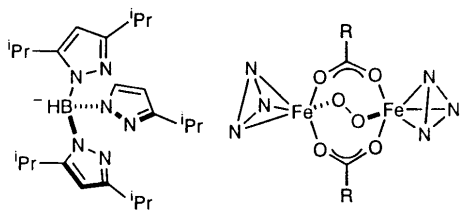

Fig. 5. A representation of the μ-1,2-peroxodiferric complex derived from 3,5-diisopropyl trispyrazoylborate.

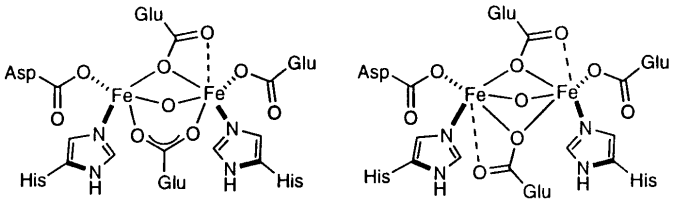

Fig. 6. Proposed core structures for intermediate X in RNR that could account for a short Fe···Fe distance.

electron-nuclear double resonance (ENDOR), stopped-flow absorption, and rR spectroscopy, a metastable species, X, was identified and characterized in the assembly of the R2 cofactor from apo-protein, ferrous ion, O_2, and reductant (Eq. (1)) [36–38]. The same compound can be generated when fully reduced R2 is allowed to react with dioxygen. Stopped-flow and rapid freeze-quench (RFQ) methods indicate that **X** has a broad absorption maximum at 365 nm, is

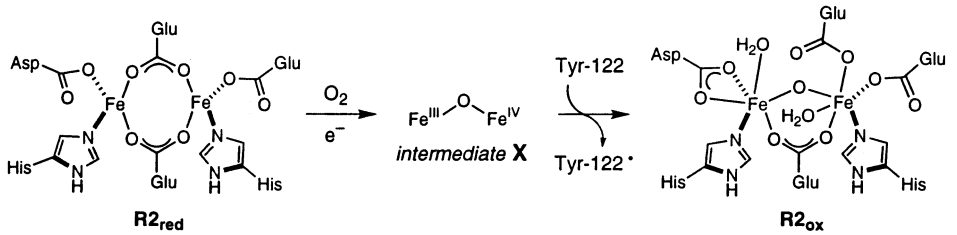

(1)

EPR active ($S = 1/2$, $g = 2.00$), and produces Tyr-122$^{\bullet}$ with a rate constant of ~ 1 s^{-1} (4°C) [37,38]. In addition, Mössbauer and ENDOR experiments reveal that **X** is composed of two inequivalent iron sites having respective isomer shifts of 0.56 and 0.26 mm s^{-1} [36,98,99]. This latter value is intermediate between those observed for high spin Fe^{3+} and Fe^{4+} in model complexes and metalloproteins. The formulation of **X** as an Fe^{3+}/Fe^{4+} pair with extensive spin delocalization on the oxygen ligands was made from ENDOR studies performed on $^{16}O_2$- and $^{17}O_2$-derived samples [99]. Results from ^{17}O ENDOR on a Y122F mutant of R2 further demonstrate that the two *O*-atoms from dioxygen are incorporated in **X**, one as a bridging oxo atom and the other a terminally bound H_2O or hydroxide. Most recently, RFQ extended X-ray absorption fine structure (EXAFS) spectroscopy has identified a short 2.5 Å Fe···Fe vector and a 1.8 Å Fe–O interaction for **X** in both wild-type and mutant R2 proteins [100]. Collectively, the experimental characterization of the R2 diiron core and reaction cycle has yielded two working models for **X** in which a mixed-valence Fe^{3+}/Fe^{4+} cluster is spanned by two carboxylates and one oxo ligand, as shown in Fig. 6.

Results from rapid freeze-quench (RFQ) Mössbauer experiments on the product of $MMOH_{peroxo}$ decay, referred to as **Q**, are consistent with the formation of a fairly symmetric diiron(IV) cluster ($\delta_1 = 0.21$ mm s^{-1}, $\Delta E_{Q1} = 0.68$ mm s^{-1} and $\delta_2 = 0.14$ mm s^{-1}, $\Delta E_{Q2} = 0.55$ mm s^{-1} from *M. capsulatus* (Bath); $\delta = 0.17$ mm

s^{-1}, $\Delta E_Q = 0.53$ mm s^{-1} from *M. trichosporium* OB3b) [85]. In addition, a short Fe···Fe distance of ~ 2.5 Å, determined by EXAFS spectroscopy, has been taken as evidence of a multiply bridged, high-valent dinuclear core (Eq. (2)) [102]. Predicted structures of **Q** together with proposed mechanistic models for alkane hydroxylation have been generated through computational studies. The following section discusses briefly some of these theoretical models.

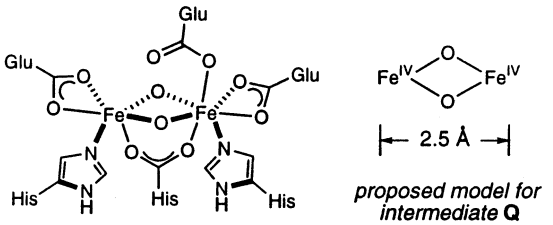

(2)

2.8.1. Siegbahn/Crabtree

A density functional theory (DFT) analysis of the mechanism for methane oxidation by MMOH was performed on a model of the active site in which two irons were bridged by formate (Scheme 2) [103,104]. The remainder of the coordination sphere on each iron site was completed with hydroxyl and water ligands. These studies support the assignment of **Q** from experiment as a bis(μ-oxo)diiron(IV) species, which is suggested to form by homolysis of a μ-1,2-peroxide. This species was excluded, however, as the oxidant responsible for methane to methanol conversion based on thermochemical calculations. The authors propose **Q** to be in equilibrium with a species containing a coordinated oxyl radical, $Fe^{III}(\mu\text{-}O)Fe^{IV}\text{–}O^{\bullet}$, which is capable of abstracting $H^{\bullet}$ from CH_4 to yield a caged $CH_3^{\bullet}$. Rapid recombination of the methyl radical with the Fe(IV) center forms an $Fe^{V}(OH)(CH_3)$ intermediate that can reductively eliminate MeOH. An assumption that underlies this proposal is that the caged $CH_3^{\bullet}$ must have an extremely short lifetime. Results from radical clock and chiral ethane experiments with MMOH from *M. trichosporium* OB3b and *M. capsulatus* (Bath) have set a lower limit of $\sim 10^{-12}$ s on the half-life for a radical intermediate on the reaction coordinate [105–110]. These experimental observations argue strongly against a radical rebound mechanism. The authors propose that H-atom abstraction occurs syn-

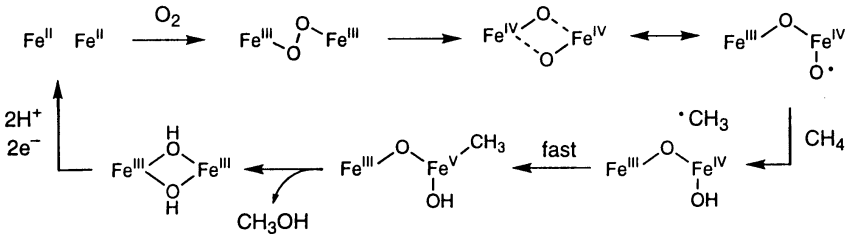

Scheme 2.

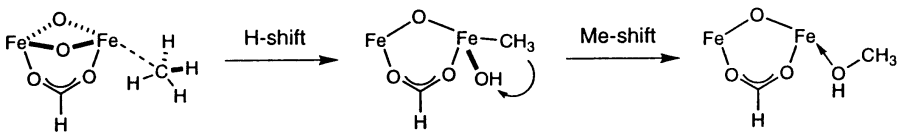

Scheme 3.

chronously with Fe–C bond formation. The generation of an alkyl iron complex is an intriguing proposal and has been suggested previously in related model oxidation chemistry and in other enzymatic reactions [111–113]. To date, no molecular systems have been synthesized to examine the reductive elimination of hydroxy- or alkoxy-iron alkyl species.

An extension of this work to include as part of the calculations all of the amino acid side chain residues in the first coordination shell of the diiron active site was recently described [114]. Refinement of this model yielded a structure for intermediate **Q** that consists of two 1,3-bridging carboxylates and two μ-oxo units. The coordination spheres of both iron atoms are completed by carboxylate and imidazole ligands. No H_2O molecules occupy the first shell of the iron core, a feature that was included in an alternative computational study (vide infra) [115]. The presence of four bridging ligands gives rise to a sufficiently short Fe···Fe distance (ca. 2.5 Å) to be consistent with data from EXAFS spectroscopy on **Q** from *M. trichosporium* OB3b [102]. Theory indicates that the two Fe(IV) centers must be antiferromagnetically coupled in order for the diiron core to possess such a small metal–metal separation, in accord with experimental data that demonstrate intermediate **Q** to have a diamagnetic ground state. Finally, these calculations suggest that CH_4 oxidation by **Q** occurs through a pure hydrogen atom abstraction pathway followed by an extremely fast recombination step that is exothermic by 63 kcal mol^{-1}. Such a mechanistic proposal is claimed to be consistent with large measured kinetic isotope effects in reactions with MMOH and with experiments based on the oxidation of chiral ethane [106,109,116].

2.8.2. Yoshizawa/Hoffmann

A two-step, concerted mechanism has been proposed for the oxidation of methane to methanol by sMMO (Scheme 3) [117,118]. The model is based on the gas-phase reaction between FeO^+ and CH_4, taken as a minimalist's approach to the enzymatic process. DFT calculations have yielded detailed energy coordinate diagrams of probable reaction pathways for these two substrates. Formation of a unique $OFe–CH_4$ adduct is believed to constitute the initial step in this process. The coordination of CH_4 to the electrophilic iron center distorts the methane molecule from T_d to either C_{3v} or D_{2d} symmetry and results in a weakening of the C–H bonds. This reduction in C–H bond strength is ascribed principally to an interaction that involves significant electron donation from the CH_4 HOMO ($\sigma_{C–H}$) to empty *d*-orbitals on iron [119,120]. The activation energy is thereby lowered to a four-centered transition state in which O–H bond formation occurs simultaneously

with C–H bond scission. Reductive elimination of the resulting HO–Fe^{+}–CH_3 intermediate affords the product complex, $Fe^{+}(HOCH_3)$.

This mechanistic model has been extended to include a diiron compound with an $Fe_2^{IV}(\mu\text{-}O)_2$ core, a putative structure for intermediate **Q** [121]. Both iron centers in **Q** are assumed to be five-coordinate. A tetra-aquated, formate-bridged $Fe_2(\mu\text{-}O)_2$ construct was used to simulate this intermediate. Extended Hückel and DFT analyses support the coordination of a C_{3v}- or D_{2d}-distorted methane molecule to one of the iron atoms through either an η^3- or η^2-binding mode, respectively. The η^2 mode is significant because it allows for inversion at carbon through a planar D_{4h} transition state [122]. Such an inversion mechanism could explain the partial scrambling of stereochemistry noted in chiral ethane experiments with sMMO without having to invoke a radical rebound-type mechanism. By analogy to the FeO^{+}/CH_4 gas-phase reaction, a concerted hydrogen shift from CH_4 to one of the μ-oxo ligands generates a μ-HO–Fe–CH_3 species, poised to eliminate MeOH.

The involvement of five-coordinate carbon intermediates in heme and non-heme oxidase reactions has been postulated [123]. In such a model, C–H oxidation is suggested to result from direct attack of a C_{3v}-distorted carbon center on an Fe=O oxygen (Eq. (3)). Related mechanistic proposals have been made for the oxidation of CH_4 by sMMO. These models are based on the concept that *O*-atom transfer occurs through a concerted or concerted asynchronous process from an oxo ligand in **Q** to a pentacoordinate methane molecule [124–126]. Alternative theoretical constructs, however, suggest that $FeO\cdots CH_4$ coordination is not an attractive interaction and, thus, does not lead to C–H activation [121,127].

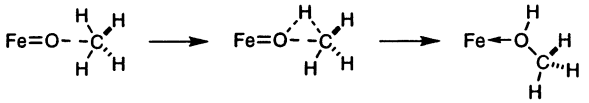

(3)

2.8.3. Friesner/Lippard

Large scale ab initio DFT calculations have generated highly evolved models for the intermediates in the sMMO catalytic cycle and have provided unique insights into the structures of these reactive species [115]. The reliability of the quantum chemical methods employed in these studies was demonstrated by reproducing the X-ray crystallographic structures of both the reduced diiron(II) and oxidized diiron(III) states of MMOH. These models contain ca. 100 atoms and preserve key hydrogen bonding patterns in the protein active site identified by X-ray crystallography. Smaller models were unable to simulate adequately the constraints imposed on the diiron core by this peripheral H-bonding network. The increased size of the computational model employed in these studies relative to pre-existing constructs requires fewer artificial restraints be placed on the system and, thus, quantitative structural comparisons to the enzyme are possible.

The structures of the two observable intermediates in the sMMO catalytic cycle, H_{peroxo} and **Q**, were examined and plausible geometries for both have been derived. The proposed structures contrast rather dramatically with existing models for these

species. Specifically, the presence of a coordinated H_2O molecule as a hydrogen-bond donor is implicated as a key component for the assembly of both H_{peroxo} and **Q**. In each complex, the H_2O ligand is bound to Fe(1) (Eq. (4)) and donates hydrogen bonds from both H-atoms. The model for H_{peroxo} displays a

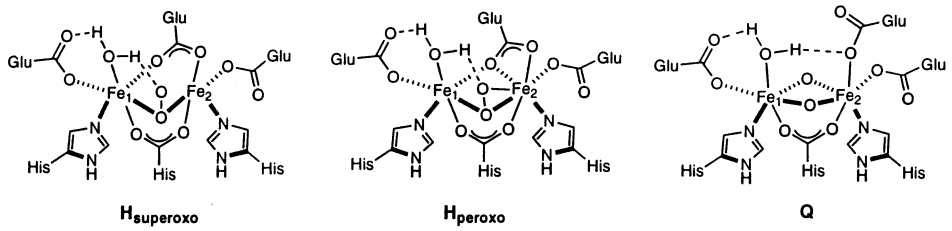

(4)

bridging O_2^{2-} unit unsymmetrically coordinated to both iron centers. One of the peroxide oxygen atoms is positioned appropriately to accept a hydrogen bond from the ligated H_2O molecule. A second H-bond contact is observed between Fe(1)–OH_2 and a terminal, monodentate carboxylate ligand (Glu-114). The positioning of a H_2O molecule on Fe(1) adds greatly to the stability of the H_{peroxo} intermediate relative to the diferrous precursor. The presence of this hydrogen-bonding network thus provides some of the thermodynamic driving force necessary for H_{peroxo} formation. The model for intermediate **Q** maintains a similar pattern of hydrogen bonding. The minimized structure has two oxo groups and a single carboxylate spanning both Fe(IV) centers. Glu-243 has shifted from a 1,1-bridging position to a monodentate coordination geometry in the structure of **Q**. This carboxylate group and Glu-144 both serve as H-bond acceptors for the coordinated H_2O, thereby contributing to the overall stability of the $Fe_2(O)_2$ core and making the conversion from H_{peroxo} to **Q** a thermodynamically downhill process.

An additional finding from these investigations offers support for the existence of a superoxide intermediate in the catalytic cycle of MMOH. The calculations suggest that such a species would be isoenergetic with H_{peroxo} and that the barrier for interconversion from $H_{superoxo}$ to H_{peroxo} would be low. This conclusion is supported by recent experimental work with MMOH from *M. capsulatus* (Bath), which indicates the presence of a kinetically detectable intermediate in the step preceding H_{peroxo} formation [84]. As observed in the model of H_{peroxo}, the apparent stability of $H_{superoxo}$ is due in part to the presence of a hydrogen bond between the O–O moiety and the Fe(1)–OH_2 group (Eq. (4)). A minimal structural change is required to convert $H_{superoxo}$ to H_{peroxo}, consistent with the evidence that these two intermediates are energetically equivalent. The findings from this computational study point to the essential function of hydrogen bonding interactions in both the first and second shell of the iron coordination sphere, features that have not been considered to date in other theoretical constructs. In order to reproduce the catalytic chemistry of MMOH in a small molecular system, it may be necessary to account for such H-bonding interactions within the model design [128,129].

3. Dinuclear iron model systems

3.1. General

The desire to elucidate the extraordinary chemistry of diiron proteins has inspired efforts to prepare molecular complexes that reproduce both the structure and function of their metallocofactors. The earliest explorations directed at the synthesis of non-heme dinuclear iron model compounds can be traced to work published in 1983 [130,131]. Thirteen years later research in three groups culminated in the crystallographic characterization of three novel 1,2-peroxodiiron(III) derivatives [89,132,133]. These complexes are putative models for the peroxo intermediate generated in the sMMO, R2, and Δ^9D reaction cycles. A detailed spectroscopic and theoretical investigation of one of these peroxo species has provided additional insight into the reactivity properties of $Fe_2(O_2)$ compounds [96]. Such studies, together with the design and synthesis of new diiron complexes, continue to advance our understanding of the protein machinery. The following sections will highlight recent efforts to construct well-defined diferrous model systems, including an account of the corresponding reaction chemistry of these adducts. Several informative reviews on this and related topics are available [3,14,15,134]; we therefore restrict our discussion to work described following the initial reports of diferric peroxides (ca. 1990) and to systems with properties that can be correlated to the biological targets of interest.

3.2. Ferrous models

3.2.1. Tris(pyrazoyl)borate

Mononuclear complexes derived from the tripodal capping ligand tris(3,5-diisopropylpyrazoyl)borate, ($HB(3,5\text{-}^iPr_2pz)_3^-$), and a carboxylate display unique reactivity with dioxygen [135]. X-ray analysis of one such adduct recrystallized from CH_3CN, $[Fe(OBz)(CH_3CN)\{HB(3,5\text{-}^iPr_2pz)_3\}]$, reveals that the metal can adopt a distorted octahedral structure by adding a solvent molecule to its coordination sphere. Many other small exogenous ligands such pyridine and DMSO can associate with the Fe^{2+} center, as evidenced by ^{1}H-NMR spectroscopy. Access to an open coordination site in $[Fe(OBz)(HB(3,5\text{-}^iPr_2pz)_3)]$ (**1**) is essential for reactivity with O_2; the sterically hindered *t*-butyl and 1-adamantyl carboxylate complexes are inert towards O_2-dependent oxidation. At low temperature (< -50°C) and in non-coordinating solvents, exposure of **1** to 1 atm of dioxygen results in the generation of an intensely blue-green colored species **2**. UV–vis spectroscopic analysis of **2** shows a broad absorption band centered at 682 nm ($\varepsilon = 3450$ cm^{-1} M^{-1} Fe_2^{-1}) that is assigned as a peroxo $\rightarrow Fe^{3+}$ charge-transfer (LMCT) transition (Fig. 7) [135]. Between -50 and -20°C, this O_2 adduct appears to form reversibly, as indicated by regeneration of the UV–vis spectrum of **1** upon purging with argon or application of a vacuum. Other *para*-substituted aryl and small alkyl (e.g. AcO^-, $EtCO_2^-$) carboxylates display similar reactivity. The temperature sensitivity of the dioxygen adduct **2** becomes apparent at or above -20°C. Slow

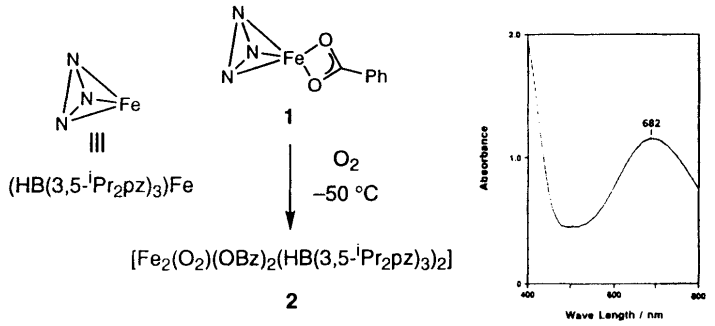

Fig. 7. Generation of peroxodiferric adduct 2 from [Fe(OBz)(HB(3,5-^{i}Pr$_2$pz)$_3$)] (**1**).

decomposition of **2** results in the generation of a red-brown solution from which dark green colored crystals slowly deposit. X-ray analysis of this material reveals a linear ferric trimer **3** (Eq. (5)). In this structure, two flanking iron atoms are each triply bridged to a central ferric ion by two benzoate ligands and either one μ-oxo or μ-hydroxo group. Studies to determine the origin of the oxo and hydroxo moieties in this complex have not been reported.

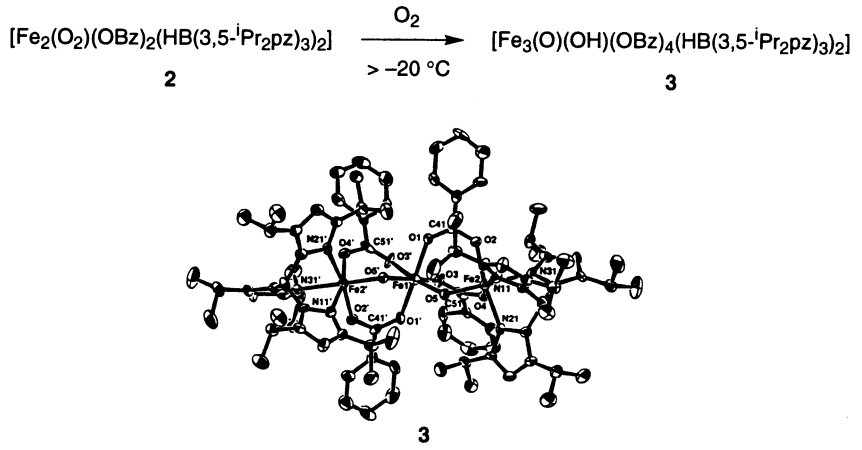

(5)

The formulation of the metastable blue-green intermediate **2** as a 2:1 metal-to-dioxygen adduct was first evidenced by manometric measurements. Subsequently, X-ray analysis was performed on an analog of **2**, [Fe$_2$(O$_2$)(O$_2$CBn)$_2$(HB(3,5-^{i}Pr$_2$pz)$_3$)$_2$] (**4**) (Fig. 8). The structure of **4** shows two {(HB(3,5-^{i}Pr$_2$pz)$_3$)Fe}$^{2+}$ units linked by a μ-1,2-peroxo ligand and two μ-1,3-phenylacetates. An Fe···Fe separation of 4.004(4) Å was determined for **4** along with O–O and Fe–O average bond distances of 1.408(9) and 1.885(12) Å, respectively [89]. The gauche Fe–O–O–Fe dihedral angle of 52.9° is quite unique and may account for spectroscopic differences between this compound and other 1,2-peroxodiferric species. The crystal structure of **4** differs from the one proposed originally for the parent complex **2**

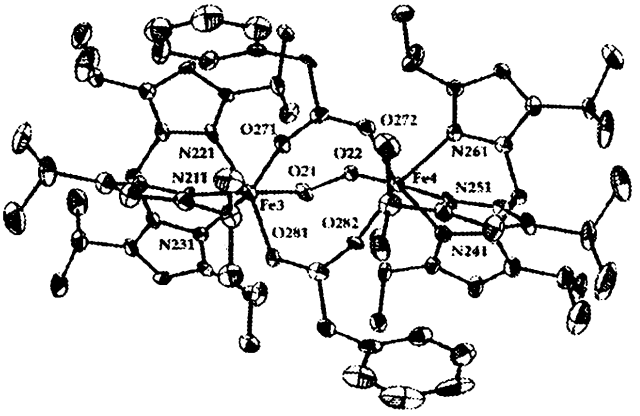

Fig. 8. X-ray crystal structure of $[Fe_2(O_2)(O_2CBn)_2(HB(3,5\text{-}^iPr_2pz)_3)_2]$ (**4**).

[135]. Based on EXAFS results and the presence of a chelating benzoate in the starting ferrous material, it was postulated that each carboxylate coordinated in a bidentate mode to each iron center. EXAFS analysis also suggested a Fe–O–O–Fe dihedral of $\sim 90°$ in **2** and gave an estimated Fe···Fe distance of 4.3 Å. The former conclusion was supported by variable temperature magnetic susceptibility data that are indicative of relatively weak antiferromagnetic coupling ($J = -33\ cm^{-1}$) in a high-spin diferric system ($\mu_{eff} \sim 4.8\ \mu_B$). A thorough spectroscopic and theoretical investigation of $[Fe_2(O_2)(OBz)_2(HB(3,5\text{-}^iPr_2pz)_3)_2]$ (**2**) has been described recently, however, which suggests that the structures of **2** and **4** are equivalent.

The rR spectrum of **2**, measured at 77 K with excitation at 647 nm, is dominated by two bands at 876 and 421 cm^{-1} [135]. In samples prepared with $^{18}O_2$, both features shift to 828 and 409 cm^{-1}, respectively. These bands have been assigned to the symmetric ν(O–O) and ν(Fe–O) stretching modes of the $Fe_2(O_2)$ core. Although the high O–O frequency suggests a strong O–O bond, a recent study argues against drawing such a conclusion. Through a combination of absorption, magnetic circular dichroism (MCD), and rR spectroscopy, four peroxide O–Fe CT transitions below 285 nm were assigned in the optical spectrum [96]. From these experimental data and density functional calculations on $[Fe_2(O_2)(O_2CH)_2(NH_3)_6]^{2+}$, a detailed electronic description of the Fe–peroxide bonding has been formulated. Salient findings from this investigation are summarized as follows: (1) peroxide binding to both ferric ions splits the O_2^{2-} π^* orbital into two non-degenerate levels, designated π_σ^* and π_π^*; (2) dominant bonding interactions in $Fe_2(O_2)$ involve the Fe(d_{yz})–peroxide(π_π^*) and Fe(d_{z^2})–peroxide(π_σ^*) orbitals; (3) the π_π^* contribution to the $O_2^{2-} \rightarrow$ Fe charge donation amounts to 50–65%; and (4) the contribution from π_σ^* donation is significantly smaller than in *trans*-μ-1,2-peroxide dicopper complexes [136]. As a result of the strong π-bonding interaction in **2**, the O–O and symmetric Fe–O stretching motions are mixed significantly. Coupling of these modes lowers the effective reduced mass for each *O*-atom, thus leading to the high observed ν(O–O).

Normal coordinate analysis (NCA) has been employed to calculate O–O bond force constants, k, in both dinuclear iron and copper peroxide complexes. By using the observed Raman data for **2** and structural parameters from the phenylacetate analog **4**, k_{O-O} was determined to be 3.07 mdyn $Å^{-1}$. The value of k_{O-O} is almost identical to that calculated for a *trans*-μ-1,2-peroxide Cu dimer **5** ($k_{O-O} = 3.10$ mdyn $Å^{-1}$), although the O–O stretching frequency is only 832 cm^{-1} for this compound. The results obtained from NCA thus support the conclusion that **2** does not have an anomalously strong O–O bond, as the high O–O stretching frequency might suggest. The k_{O-O} and ν(O–O) in a dicopper $\mu-\eta^2:\eta^2$-peroxide **6** are substantially lower at 2.4 mdyn $Å^{-1}$ and 763 cm^{-1}, respectively. This difference has been attributed to favorable Cu → peroxide(σ*) back-bonding in **6**, an interaction that is not evident in the molecular orbital description of either **2** or **5** [137,138]. The absence of an Fe → peroxide(σ*) contribution to bonding in 1,2-bridging diferric peroxides may reflect the reactivity of such species.

The similarity in k_{O-O} for **2** and **5** indicates that an approximately equal amount of charge resides in the π* orbitals of the O–O unit in both complexes [96]. This proposal does not seem unreasonable considering the differences in the relative contributions of the π_π^* and π_σ^* from O_2^{2-} to the metal-peroxide bond (vide supra). Reactivity studies on the Cu dimer **5** have demonstrated that the O–O unit is strongly basic and can serve as a nucleophile; therefore, it has been suggested that **2** has similar properties [139]. Investigations into the protonation and subsequent decomposition behavior of **2** remain to be conducted.

3.2.2. N_6O dinucleating ligands

Polypyridyl- and polyimidazolyl-based ligands with a single bridging phenoxyl or alkoxyl group furnish kinetically stable diiron complexes (Fig. 9) [140,141]. These N_6O systems chelate each metal center forming either five- or six-membered rings between a tertiary amine donor and the *O*-atom bridge. With this ligand construct, it is possible to position two metal ions within ~3.5 Å of one another. Moreover, both pyridine and imidazole units can be substituted to create a steric cavity in which the metal centers are encapsulated. The importance of this latter design feature for preventing the bimolecular decay of reactive oxygenated intermediates will be highlighted later in the discussion.

Reaction of $Fe(BF_4)_2 \cdot 6H_2O$ with Ph-bimp **7** and NaOBz under anaerobic conditions affords a 1,3-benzoate-bridged diferrous adduct **8** [132,142]. This complex contains two five-coordinate Fe^{2+} centers and reacts readily with O_2 (CH_3CN, 20°C) to give an intensely green-colored solution. An optical spectrum of this oxygenated species **9** shows a broad absorption band between 500 and 800 nm ($\varepsilon \sim 1700$ cm^{-1} M^{-1}, Fig. 10). Boiling the reaction mixture restores the spectrum of the starting diferrous complex **8**. The reversible oxygenation of **8** can be cycled with no apparent ligand decomposition. The remarkable stability of **9** makes possible its crystallization at −20°C from a CH_3CN solution. X-ray analysis shows a triply bridged structure with a *cis*-μ-1,2-peroxide, μ-phenolate, and μ-1,3-benzoate spanning two Fe^{3+} centers. Although Ph-bimp has a C_2-axis, the complex, $[Fe_2(O_2)(OBz)(Ph\text{-}bimp)](BF_4)_2$ (**9**), assembles with two inequivalent six-coordinate

ferric sites as seen from both the crystal structure and Mössbauer data. Accordingly, the Fe–$O_{peroxide}$ bond lengths are 1.864(4) and 1.944(4) Å; the Mössbauer spectrum collected at 77 K on a powdered sample shows two sets of quadrupole doublets ($\delta_1 = 0.58$ mm s^{-1}, $\Delta E_{Q1} = 0.74$ mm s^{-1}; $\delta_2 = 0.65$ mm s^{-1}, $\Delta E_{Q2} = 1.70$ mm s^{-1}). These parameters are indicative of high-spin ferric centers that, together with the observed O–O bond length of 1.426(4) Å, establish **9** as a diferric peroxide [132].

Reversible oxygenation activity is not exclusive to **8** and is observed in other N_6O ligand-derived ferrous complexes. In the tetrapyridyl series tpdp, Me_2-tpdp, and

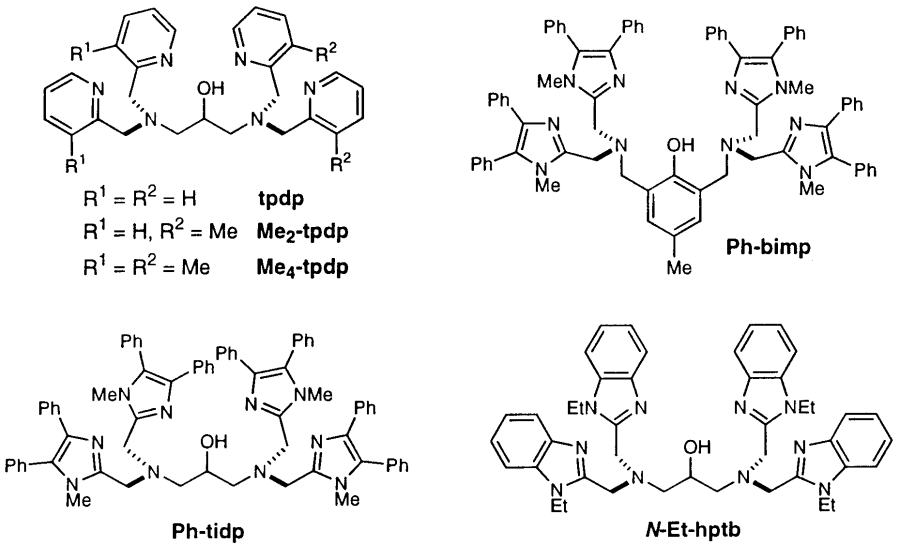

Fig. 9. A collection of polypyridyl and polyimidazole ligands used for the preparation of dinuclear iron adducts.

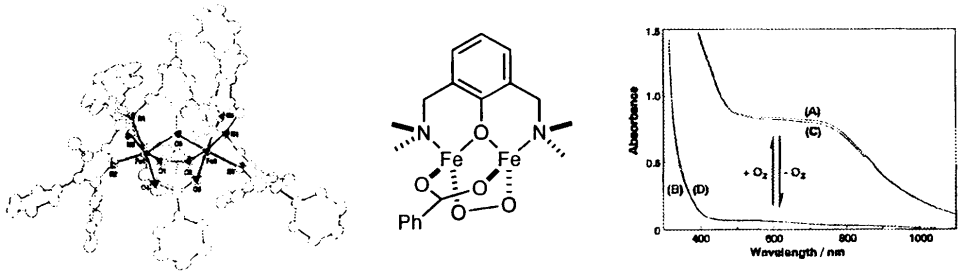

$[Fe_2(O_2)(OBz)(Ph\text{-}bimp)](BF_4)_2$

9

Fig. 10. Crystal structure and UV–vis spectrum of diferric peroxide **9** prepared from Ph-bimp.

Me_4-tpdp (Fig. 9), dioxygen reactivity and peroxide stability can be correlated to changes in the ligand structure and donor atom strength [140,143]. Reaction of $[Fe_2(OBz)(tpdp)]^{2+}$ (**10**) with O_2 at -40°C leads to an instantaneous, irreversible decomposition. The equivalent complex prepared from Me_2-tpdp **11** produces an oxygenated adduct at -60°C that breaks down slowly at this temperature. Introduction of two more *ortho*-methyl substituents affords $[Fe_2(OBz)(Me_4$-tpdp$)]^{2+}$ (**12**) and results in a dramatic increase in the stability of the corresponding peroxide species **13**. Compound **13** is generated and does not decompose at -30°C. Unlike other tpdp-based systems, this adduct can be reverted to its deoxy form by bubbling argon gas through the cold solution. At ambient temperature, however, **13** reacts to give as yet unidentified, brown products. Oxygenated complexes derived from the polyimidazole ligand, Ph-tidp, demonstrate much greater resistance to decay than any of the tetrapyridyl systems. As an example, $[Fe_2(O_2)(OBz)$(Ph-tidp)$]^{2+}$ (**14**) can be deoxygenated by warming from low temperature to 23°C and the corresponding ferrous compound is recovered quantitatively.

The X-ray structure of $[Fe_2(O_2)(OBz)$(Ph-bimp)$](BF_4)_2$ (**9**) reveals a O_2^{2-} ligand buried deeply within a cavity formed by the phenyl groups [132]. Molecular models of the tpdp ligands indicate that *ortho* substitution on the pyridine rings, specifically in Me_4-tpdp, produces a similar pocket in which to house the O_2 unit. The placement of a methyl group in the 6-position of the pyridine and two phenyl substituents on the imidazole ligands also has a significant influence on the Fe–N distances and on the coordination geometry of the iron centers. For example, the average Fe–N length observed in a crystal structure of **12** is elongated by ~ 0.1 Å relative to unsubstituted Fe-polypyridyl complexes. A direct comparison of the $E_{1/2}$ values measured for diferrous adducts $[Fe_2(O_2CCF_3)(Me_2$-tpdp$)]^{2+}$ and $[Fe_2(O_2CCF_3)(Me_4$-tpdp$)]^{2+}$ (420 and 640 mV vs. SCE in CH_3CN, respectively) attests to the influence steric interactions have on the donor ability of these particular systems. The weakened electron donor strength of the Me_4-tpdp and Ph-bimp ligands favors the Fe^{2+} oxidation state, thereby facilitating deoxygenation of the diferric peroxide species. Consistent with this tendency, the dioxygen binding affinities of these complexes increase in order of increasing donor ability of the bridging carboxylate.

Resonance Raman spectra have been recorded for photolabile tpdp-based peroxide adducts [143]. Data collected on the oxygenated complex of **12** in CH_2Cl_2 (-40°C) shows an O–O stretching frequency at 918 and 891 cm^{-1}. The observation of two stretching frequencies has been attributed to Fermi resonance. Two bands at 450 and 486 cm^{-1} are assigned to symmetric and antisymmetric Fe–O stretches and indicate that the $Fe_2(O_2)$ core does not have a center of symmetry. This finding suggests that the iron atoms are inequivalent in $[Fe_2(O_2)(OBz)$-$(Me_4$-tpdp$)]$, as noted in the X-ray structure of the related adduct **9** (vide supra). When $^{18}O_2$ was used, the 450 and 486 cm^{-1} bands shift to 442 and 479 cm^{-1}, respectively; a doublet at 857 and 889 cm^{-1} appeared, corresponding to ν(O–O). The high O–O stretching frequency determined from rR spectroscopy is in accord with the properties of other known μ-1,2-peroxodiferric compounds.

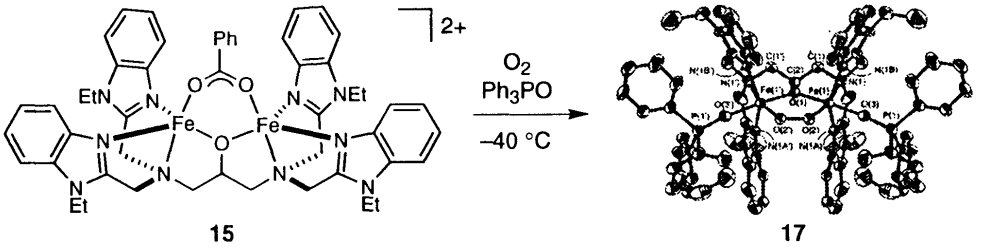

Fig. 11. Synthesis and ORTEP diagram of $[Fe_2(O_2)(Ph_3PO)_2(N\text{-Et-hptb})]^{3+}$.

A related class of N_6O benzimidazole-based ligands has been used to investigate the reaction of dioxygen with the corresponding diferrous complexes [143–145]. By analogy to the tetrapyridine and tetraimidazole systems, these compounds illustrate how incremental ligand alterations can affect the reactivity of the metal centers. One such adduct, $[Fe_2(OBz)(N\text{-Et-hptb})](BF_4)_2$ (**15**), binds O_2 irreversibly at -60°C to afford a metastable purple-blue product **16**. It was concluded from UV–vis spectroscopy that the benzoate remains bound in **16** based on an observed blue shift of the peroxo O–Fe^{3+} LMCT band from 588 to 570 nm when this group is exchanged with the more basic propionate [141]. Resonance Raman spectroscopy verifies the assignment of the 588-nm band as a LMCT transition and shows two features at 476 and 900 cm^{-1}. These bands shift to 460 and 850 cm^{-1}, respectively, with the use of $^{18}O_2$. The O–O stretching frequency at 900 cm^{-1} appears as a Fermi doublet that collapses to a single peak upon ^{18}O substitution. Although the observed isotopic shifts are in good agreement with those calculated from a simple diatomic model ($\nu_{calc}(Fe\text{–}^{18}O) = 455$ cm^{-1}; $\nu_{calc}(^{18}O\text{–}^{18}O) = 849$ cm^{-1}), the $k_{O\text{–}O}$ value of 3.26 mdyn $Å^{-1}$ determined from NCA is quite different from the value of 3.82 mdyn $Å^{-1}$ obtained if one assumes a harmonic oscillator. This property would suggest that mixing between the Fe–O and O–O stretch motions (mechanical coupling) contributes to the high ν(O–O), as is the case for $[Fe_2(O_2)(OBz)_2(HB(3,5\text{-}^{i}Pr_2pz)_3)_2]$ **2** (vide supra).

Nuclear magnetic resonance spectroscopy has been used to probe changes in the ligand conformation upon addition of donor groups [141]. From these experiments, it was concluded that Ph_3PO and Me_2SO are able to coordinate to one or both trigonal bipyramidal ferrous sites in **15**. These additives, as well as other polar aprotic reagents, have a pronounced effect on the stability of the peroxo adduct **16**. In a Me_2SO–CH_3CN mixture, **16** is reported to persist for ~ 30 min at ambient temperatures. The addition of Ph_3PO to a CH_3CN solution of **15** prior to oxygenation affords a peroxide **17** that is stable for months at -40°C. The enhanced stability of **17** allows for low temperature crystallization of this material. X-ray analysis reveals that the O_2^{2-} unit is bound in a symmetric *cis* μ-1,2 mode with an Fe–O–O–Fe dihedral angle of ~ 0° (Fig. 11) [133]. The O–O bond distance of 1.416(7) Å is consistent with a peroxide formulation and is comparable to those recorded for $[Fe_2(O_2)(OBz)_2(HB(3,5\text{-}^{i}Pr_2pz)_3)_2]$ (**2**) (1.408 Å) and $[Fe_2(O_2)(OBz)$-$(Ph\text{-bimp})](BF_4)_2$ (**9**) (1.426 Å) [89,132]. An Fe···Fe distance of 3.462(2) Å separates

the doubly-bridged, crystallographically equivalent ferric centers. Most notably, two Ph_3PO ligands have replaced the μ-1,3-benzoate ligand present in the X-ray structure of the starting compound **15**.

Original reports on the reactivity of **16** noted that 2,4-di-*tert*-butylphenol and Ph_3P do not affect the UV–vis spectrum of this compound at -50°C. Examination of the products formed upon thermolysis of these mixtures gives no evidence of biphenol; however, $\sim 10\%$ of Ph_3PO is detected in the ^{31}P-NMR [141]. By contrast, 2,4-di-*tert*-butylphenol and Ph_3P do accelerate breakdown of a related tetrapyridyl adduct, $[Fe_2(O_2)(OBz)(tpdp)]^{2+}$ (**18**), at -50°C [140]. The reaction of **18** with the substituted phenol affords 50% of the coupled product, whereas $\sim 60\%$ of Ph_3P is converted to the corresponding oxide. These results may represent unique examples of oxidation reactions promoted by a discrete diferric peroxide **18**; however, the mechanisms of these processes are unknown.

The decomposition pathway of peroxides **16** and **17** has been speculated to involve as a first step O–O bond homolysis to give a bis(Fe^{IV}=O) species [133]. Substitution of the more donating benzoate ligand with neutral phosphine oxides decreases electron density at the metal centers and disfavors the iron(IV) oxidation state, providing a convenient rationalization for the increased stability of **17** over **16**. The rate of peroxide decay can be modulated by the introduction of *meta*- and *para*-substituents on the bridging benzoate. A plot of $\log k_{obs}$ versus Hammett σ values shows a linear correlation with a ρ of -1.1. Thus, decomposition of $[Fe_2(O_2)(OCH_2Ar)(N\text{-Et-hptb})]^{2+}$ is slowed by electron-withdrawing groups, lending some support to the proposed mechanism for peroxide decay. Examination of the temperature dependence of the breakdown of **16** affords activation parameters, $\Delta H^{\ddagger} = 15.5 \pm 0.8$ kcal mol^{-1} and $\Delta S^{\ddagger} = -11 \pm 5$ eu, that are consistent with values determined in O–O cleavage reactions of other peroxide compounds [146]. A detailed kinetic analysis on the decay of $[Fe_2(O_2)(OBz)(N\text{-Et-hptb})]^{2+}$ (**16**) has been described, however, that argues against a unimolecular decomposition pathway involving $Fe^{IV} = O$ intermediates [146,147]. According to this report, a solution of **16** in either CH_3CN or EtCN is indefinitely stable at or below -35°C. When **16** is warmed to room temperature, a slow bleaching of the peroxide LMCT band centered near 600 nm results to give a featureless UV–vis spectrum. The final product(s) from the thermolysis reaction contains iron at the ferric oxidation level and is assumed to be predominantly tetranuclear material, based on the crystallographic characterization of one such species **19**. Manometric measurements demonstrate that only half the number of moles of O_2 taken up in the oxygenation step have been consumed after decomposition is complete. By systematically varying the concentrations of dioxygen and the diferrous complex, a second-order dependence on **16** for this decay process was fit accurately to the experimental data. Collectively, these findings support a disproportionation mechanism that yields one equivalent of O_2 and either two equivalents of a dinuclear ferric complex or one equivalent of a tetranuclear complex (Scheme 4). The bimolecular decay of **16** (and related N_6O diferric peroxides) can be explained through two reasonable reaction pathways. Dissociation of an $Fe\text{–}O_{peroxide}$ bond in **16** upon warming could lead to generation of either a tetrairon mono- or bis-peroxide species, depending on where

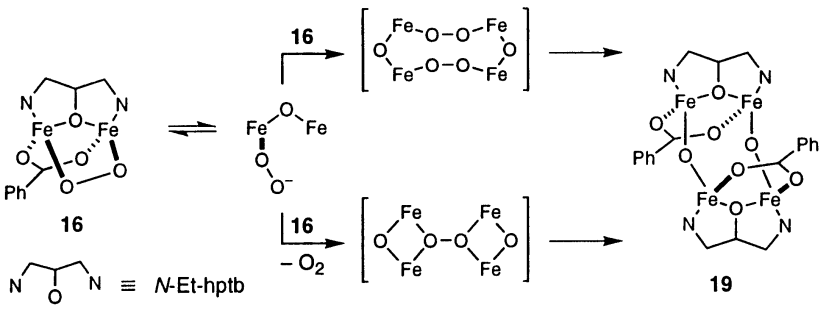

Scheme 4.

along the reaction coordinate O_2 is liberated. Either of these intermediates would convert subsequently to **19**. Alternatively, although dioxygen binding to **16** is observed to be irreversible at low temperature, collision between two molecules of **16** may produce enough kinetic energy to cause O_2 to dissociate. Once O_2 is released, the resulting diferrous material could reduce the O–O bond of the peroxide complex to yield the product **19**. The details of decomposition mechanism notwithstanding, these results underscore the importance of designing ligand systems that sufficiently isolate reactive dioxygen species in order to subvert second-order decay processes.

3.2.3. H_2XDK

The dicarboxylate ligand *m*-xylylenediamine bis(Kemp's triacid)imide, H_2XDK (**20**), provides an ideal platform upon which to bind and stabilize kinetically two metal ions [148–150]. Highly efficient syntheses have been described for bis(μ-1,3-carboxylate) diferrous complexes from **20** and related adducts from H_2PXDK (**21**) and H_2BXDK (**22**) (Fig. 12). These models incorporate two additional carboxylate ligands and two aromatic *N*-donors, thus reproducing the exact composition of the protein ligand environment found in most diiron enzymes. The unique arrangement of ligands in these compounds, as exemplified by [Fe_2(μ-PXDK)(μ-O_2C^tBu)(*N*-MeIm)$_2$(O_2C^tBu)] (**23**), places one ferrous site in an octahedral geometry (Fe1) while leaving the second metal coordinatively unsaturated (Fe2) [151,152]. In

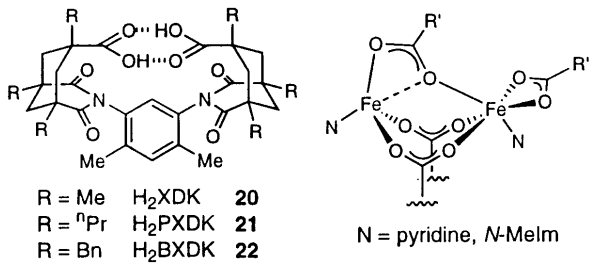

Fig. 12. Schematic of the diferrous complexes derived from the XDK ligands.

addition to the μ-1,3-carboxylates from the XDK dianion, a third RCO_2^- unit links Fe1 and Fe2. The binding mode of this ancillary carboxylate is best described as a hybrid of the *syn–anti* and *syn–syn* canonical forms. An average metal–metal separation of ~ 3.6 Å has been determined for the triply-bridged core in six homologous structures.

Mössbauer spectra collected on **23**, $[Fe_2(\mu\text{-BXDK})(\mu\text{-}O_2CPhCy)(O_2CPhCy)(C_5H_5N)_2]$ (**24**), and $[Fe_2(\mu\text{-BXDK})(\mu\text{-}O_2CPhCy)(O_2CPhCy)(N\text{-MeIm})_2]$ (**25**) ($CyPhCO_2^-$ = 1-phenylcyclohexanecarboxylate) indicate that these complexes remain dinuclear in solution as dimetallic units. Polycrystalline samples of **23** at 20 K display two sets of quadrupole doublets with isomer shift and quadrupole splitting values ($\delta_1 = 1.34$ mm s^{-1}, $\Delta E_{Q1} = 2.94$ mm s^{-1}; $\delta_2 = 1.15$ mm s^{-1}, $\Delta E_{Q2} = 3.17$ mm. These results differ minimally from data obtained on material frozen in THF ($\delta_1 = 1.36$ mm s^{-1}, $\Delta E_{Q1} = 3.02$ mm s^{-1}; $\delta_2 = 1.14$ mm s^{-1}, $\Delta E_{Q2} = 3.15$ mm s^{-1}). These parameters are consistent with high spin ferrous ion and match closely those values obtained for the reduced forms of MMOH ($\delta = 1.30$ mm s^{-1}, $\Delta E_{Q1} = 2.87$ mm s^{-1}) and R2 ($\delta = 1.26$ mm s^{-1}, $\Delta E_{Q1} = 3.13$ mm s^{-1}). As expected, spectra of **24** and **25** are essentially identical to that of **23**.

The reaction of diferrous XDK compounds with dioxygen has been interrogated by UV–vis, EPR, Mössbauer, rR, and manometric experiments [88,152]. Initial studies demonstrated that the addition of O_2 to colorless THF solutions of **23** results in the production of a deep purple species **26** ($\lambda_{max} \sim 670$ nm). This intermediate converts rapidly to a red compound ($\lambda_{max} \sim 470$ nm), most likely a mixture of ferric products based on its convoluted Mössbauer spectrum. Decomposition of the red species occurs upon warming to yield yellow–green material having absorption bands characteristic of oxo-bridged polyiron(III) units [152]. Given the instability of these intermediates, in particular **26**, other physical measurements were not performed. Efforts to investigate further this oxygenation reaction, therefore, necessitated the construction of derivatives of **23** that would increase the lifetimes of the corresponding oxygenated products. The H_2BXDK (**22**) ligand was designed to shield better both metal centers by positioning sterically encumbering benzyl substituents proximal to the iron sites. In addition, the pivalates in **23** were replaced with the larger $CyPhCO_2^-$ and 2,4,6-triisopropylbenzoate groups. The influence of the two *N*-donors on the dioxygen chemistry of these compounds also has been explored by substituting *N*-MeIm with pyridine [88].

Exposure of $[Fe_2(\mu\text{-BXDK})(\mu\text{-}O_2C^tBu)(O_2C^tBu)(C_5H_5N)_2]$ (**27**) to O_2 at -77°C (THF) effects the slow, irreversible formation of a midnight blue species **28** with UV–vis properties characteristic of a diferric peroxide ($\lambda_{max} \sim 580$ nm, $\varepsilon \sim 1200$ M^{-1} cm^{-1}). Above -65°C, **28** decomposes within 5 min to a light brown material. Manometric measurements on analogs of **28** establish that 1.0 ± 0.1 equivalents of O_2 are consumed in these reactions. This value remains invariant regardless of whether THF, Et_2O, or CH_2Cl_2 is employed as solvent. Additional O_2 uptake (0.7–1.0 equivalents) occurs upon thermolysis of solutions of **28** in either THF or CH_2Cl_2, but not in Et_2O. These findings contrast with reports on the decay of μ-alkoxo-bridged diferric 1,2-peroxides, in which 0.5 equivalents of O_2 are liberated.

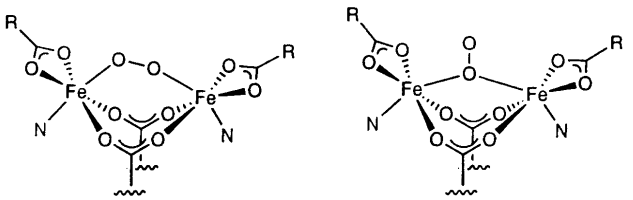

Fig. 13. Putative peroxide structures generated from diiron(II) XDK compounds.

Spectroscopic experiments confirm the assignment of the metastable blue product as a peroxodiferric complex [88]. Resonance Raman spectra collected on six different species having either pyridine or imidazole ligands (toluene, -77°C) exhibit identical O–O stretching frequencies at ν(O–O) = 864 cm^{-1}. This band shifts to ν(O–O) = 818 cm^{-1} in $^{18}O_2$-derived compounds. The frequency difference of 46 cm^{-1} matches closely the predicted value of 50 cm^{-1} for a diatomic oscillator. An O–O stretch of 864 cm^{-1} is consistent with a μ-1,2-coordination mode, although such a designation must be considered tentative without available ν(Fe–O) data and/or an X-ray crystal structure. The presence of an O_2^{2-} unit bridging Fe1 and Fe2 is also suggested from the lack of an EPR signal at 4.5 K. This property requires antiferromagnetic spin exchange between the two metal centers to give an $S = 0$ ground state, electronic coupling that is mediated most probably through the peroxide moiety. Apparent diamagnetic behavior at low temperature is observed for other $Fe_2^{III}(\mu\text{-}O_2)$ model systems and for the H_{peroxo} intermediate in the MMO reaction cycle. Additional insight into the structure of the blue species is gained from Mössbauer data on the oxygenated product of **24**. The appearance of two overlapping quadrupole doublets with $\delta_1 = 0.47$ mm s^{-1}, $\Delta E_{Q1} = 0.88$ mm s^{-1} and $\delta_2 = 0.63$ mm s^{-1}, $\Delta E_{Q2} = 1.20$ mm s^{-1} is indicative of inequivalent high spin ferric ions. Taken together, these data suggest several likely configurations for the XDK-based diferric peroxide, as depicted in Fig. 13.

A detailed kinetic examination of peroxide formation with diferrous XDK compounds illustrates the effect of intraligand steric interactions on modulating oxygenation rates [88]. Reactions of bis(pyridine) adducts (e.g. **24** and **27**) could be monitored conveniently by UV–vis spectroscopy, and are determined in all cases to be first-order in both complex and dioxygen ($k \sim 0.04$–0.16 M^{-1} s^{-1}, -77°C). Bimolecular collision between O_2 and the diferrous core, therefore, is implicated as the rate-limiting step in peroxide formation. The calculated rate constant for this event correlates with a lengthening of the Fe2-(μ-O_2CR) bonds as the R group of this ancillary carboxylate is made larger. This observation suggests that reaction of O_2 occurs initially at the coordinatively unsaturated Fe2 site, and that binding of O_2 may be coupled with a positional shift of the bridging RCO_2^- group. In addition, the reaction rates of diferrous XDK complexes with dioxygen are strongly influenced by the nature of the *N*-donors. Bis(imidazole) adducts display markedly enhanced reactivity compared to their pyridine counterparts. By using stopped-flow optical methods, a pseudo-first-order rate constant of 300 s^{-1} was measured for the oxygenation of **23**, a value five orders of magnitude larger than the corresponding value recorded for pyridine derivatives [88,152,153]. This difference has been

ascribed to the increased σ-donor strength of imidazole relative to pyridine, which should cause a significant negative shift in the midpoint potential for the Fe^{3+}/Fe^{2+} couple. Thus, the accelerated reaction rate can be correlated to the greater thermodynamic driving force for oxidation of the bis(imidazole) complex. A similar effect has been noted in carboxylate-bridged hexaamine compounds that bind dioxygen reversibly (vide supra).

The intrinsic potential of XDK-based diferric peroxides to promote substrate oxidation has been probed by using numerous reagents such as Ph_3P, phenols, alkenes, and saturated hydrocarbons [153]. Deep blue oxygenation adducts produced from [Fe_2(μ-BXDK)(μ-O_2CPhCy)(O_2CPhCy)(C_5H_5N)$_2$] (**24**) and [Fe_2(μ-PXDK)(μ-O_2CPhCy)(O_2CPhCy)(*N*-^{n}BuIm)$_2$] (**29**) were allowed to react at −77°C with varying amounts of substrates and the subsequent events were monitored by UV–vis spectroscopy and GC-MS. In certain cases, mixtures were allowed to warm to 23°C and the products then analyzed. Collectively, results from this study indicate that these peroxo species have basic/nucleophilic character and are incapable of transferring an oxygen atom to even potent acceptors such as Ph_3P. Solvent oxidation does occur, however, upon thermolysis of the blue species in THF, CH_2Cl_2, toluene, cyclopentane, and cyclohexene solutions. Four lines of evidence point to a radical autooxidation pathway as the operative mechanism for this process: (1) mixtures of both alcohol and ketone products are formed; (2) k_H/k_D values of 6.2 and 7.8 are measured for THF and toluene oxidation, respectively; (3) dioxygen is consumed upon warming of the reaction, as indicated by manometry; and (4) no oxidized materials are generated when either *n*-pentane or isopentane is employed as solvent. It was concluded, therefore, that thermolysis results in H-atom abstraction provided that the C–H bond strength is sufficiently weak (<95 kcal mol^{-1}), and that the incipient carbon radical propagates a chain reaction [111,154,155]. Clearly, this reaction pathway is distinct from that of MMO and other non-heme hydroxylases despite the obvious structural similarities between these XDK models and the diiron cofactors. The fact that the peroxide moiety is basic/nucleophilic is consistent with the prediction that H_{peroxo} in MMO has similar properties, suggesting that protonation may be a prerequisite for subsequent conversion to a high valent iron intermediate (vide infra) [53,96].

3.2.4. 2,6-Diarylbenzoic acid

The reaction of *m*-terphenyl-based carboxylic acids with ferrous salts produces novel dinuclear tetracarboxylate clusters through an efficient self-assembly process [156–159]. 2,6-Di(*p*-tolyl)- (**30**), 2,6-di(*p*-fluorophenyl)- (**31**), and 2,6-dimesitylbenzoic acid (**32**) have been utilized for this purpose (Eq. (6)). Most of the following discussion will detail experiments performed with **30**; important observations made with benzoate compounds **31** and **32** will be highlighted where appropriate.

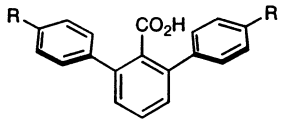

R = Me $Ar^{Tol}CO_2H$ **30**
R = F $Ar^{F}CO_2H$ **31**

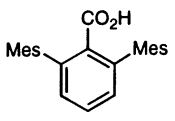

$Ar^{Mes}CO_2H$ **32**

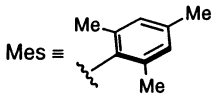

(6)

The bis(carboxylate)-bridged diferrous complex, $[Fe_2(\mu\text{-}O_2CAr^{Tol})_2(O_2CAr^{Tol})_2(THF)_2]$ **33** (Ar^{Tol} = 2,6-di(*p*-tolyl)phenyl), can be prepared by reacting two equivalents of $FeBr_2$ with the Tl^+ salt of $Ar^{Tol}CO_2H$ in THF. Complex **33** is a convenient starting material that readily exchanges both THF ligands for pyridine and imidazole [156]. By exploiting this property, it has been possible to generate unique dinuclear adducts, $[Fe_2(\mu\text{-}O_2CAr^{Tol})_2(O_2CAr^{Tol})_2(C_5H_5N)_2]$ (**34**) and $[Fe_2(\mu\text{-}O_2CAr^{Tol})_2(O_2CAr^{Tol})_2(N\text{-MeIm})_2]$ (**35**) (Scheme 5). These compounds have been characterized crystallographically and are similar in structure to that of the starting material **33**. The ferrous centers in **33**, **34**, and **35** are linked by two μ-1,3-carboxylates with a metal–metal separation of $\sim$4.3 Å. Two additional $ArCO_2^-$ ligands are bound terminally in a bidentate fashion to each iron site, with the exception of **35** in which both monodentate (**A**) and bidentate (**B**) coordination of the non-bridging carboxylates are noted. This latter finding suggests that **A** and **B** are of similar energy and that large thermodynamic barriers in such systems do not inhibit carboxylates from altering their coordination mode. The composition and arrangement of the ligands in **35** are unique and closely mimic the diferrous active-site structures of R2 and Δ^9D.

A complex related to **33** has been synthesized from dimesitylbenzoic acid **32** [155]. Reaction of Li^+-**32** with $Fe(OTf)_2$ in toluene–CH_3CN furnishes $[Fe_2(\mu\text{-}O_2CAr^{Mes})_2(O_2CAr^{Mes})_2(CH_3CN)_2]$ **36**. Each iron center in **36** is square pyramidal with the apical position occupied by a CH_3CN ligand (Fig. 14). The Fe···Fe separation of 4.122(1) Å is comparable to those observed in models derived from **30** and in the fully reduced forms of diiron carboxylate enzymes (3.9 Å for $R2_{red}$, 4.2 Å for Δ^9D). As seen in all dinuclear clusters generated from these sterically hindered carboxylates, the *ortho*-aryl groups arrange adventitiously to form the walls of a pocket that encapsulate both metal ions. Site isolation of the diferrous unit makes possible the kinetic stabilization of an otherwise labile carboxylate-rich compound.

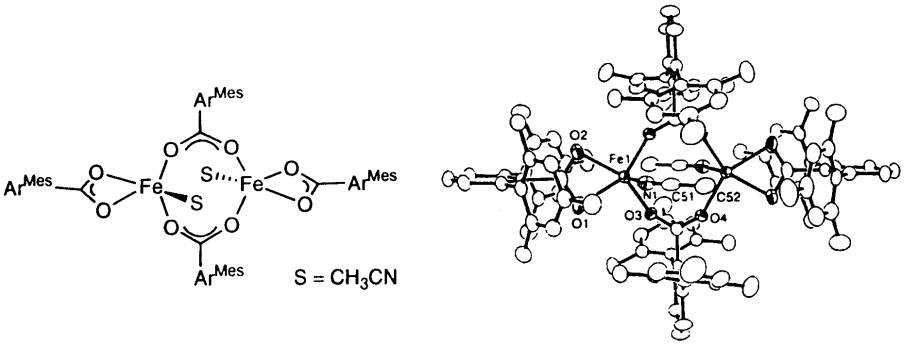

Fig. 14. X-ray crystal structure of $[Fe_2(\mu\text{-}O_2CAr^{Mes})_2(O_2CAr^{Mes})_2(CH_3CN)_2]$ (**36**).

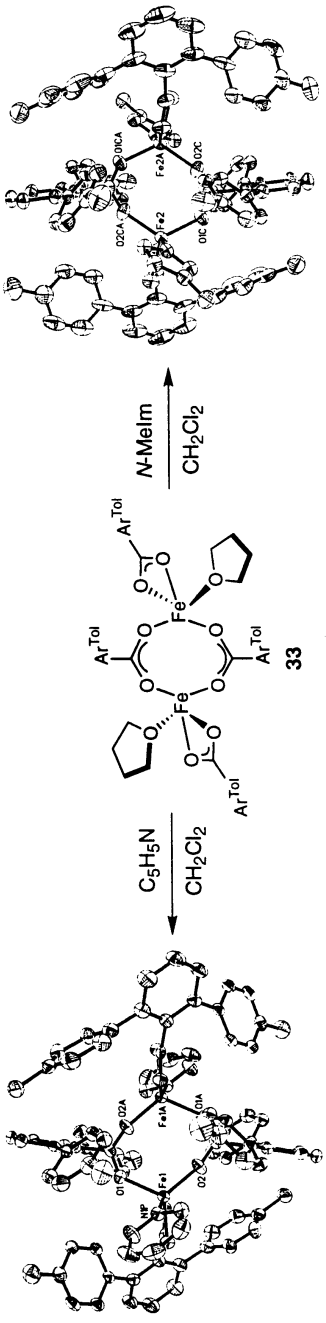

Scheme 5.

The reactivities of these diarylbenzoate complexes with O_2 are surprisingly disparate despite their structural similarities. Oxygenation of a CH_2Cl_2 solution of either **33** or **35** at -78°C generates a deep yellow species exhibiting a featureless optical absorption spectrum. No intermediate species are observed when the reaction is monitored by UV–vis spectroscopy. In contrast, reaction of **34** with O_2 at -78°C results in the formation of a deep emerald green complex **37** ($\lambda_{max} \sim 660$ nm). This intermediate decays with clean isosbestic behavior to a yellow material when the solution is warmed above ca. -60°C. The major product ($\sim 90\%$) from thermolysis has been characterized crystallographically as a novel tetrabridged diferric adduct, $[Fe_2(\mu\text{-}OH)_2(\mu\text{-}O_2CAr^{Tol})_2(O_2CAr^{Tol})_2(C_5H_5N)_2]$ (**38**). The coordination sphere of each iron center in **38** is completed with one pyridine ligand and one monodentate carboxylate. A substantially shorter Fe···Fe separation of 2.8843(9) Å than that observed in the starting material **34** (4.2822(7) Å) highlights the unique ability of this compound to accommodate significant structural alterations while remaining intact as a dimetallic unit. Two hydrogen bonds between the bridging hydroxides and the dangling oxygen atoms of the terminally bound $Ar^{Tol}CO_2^-$ ligands fix the positions of these carboxylate groups. The overall conversion of **34** to **38** with O_2 is remarkable given that the dimetallic core remains secured in the absence of any chelating units.

The identity of the green intermediate generated from **34** has been the subject of intense scrutiny [158]. Initial reactivity studies with **37** demonstrated that a species present in the solution was capable of converting 2,4,6-tri-*t*-butylphenol to the phenoxyl radical (-78°C). Formation of $ArO^{\bullet}$ was determined both by UV–vis ($\lambda_{max} = 383$, 401 nm) and EPR ($g = 2.0045$ at 77 K) spectroscopy; spin quantitation indicates a yield of $\sim 9\%$ based on iron for this process when excess phenol is employed. This reaction models precisely the functional chemistry of the R2 subunit in RNR [36].

Efforts to elucidate the physical properties of **37** have been hampered by problems encountered due to the poor solubility of **34** in non-polar solvents, thus, prompting the synthesis of related compounds with increased lipophilicity. Substitution of the THF ligands in **33** with two equivalents of 4-*t*-butylpyridine affords a yellow, crystalline material **39** that readily dissolves in CH_2Cl_2. X-ray analysis of this compound shows a dinuclear core in which four μ-1,3-carboxylates bridge two Fe^{2+} centers (Scheme 6). Both pyridine ligands cap the ends of the $\{Fe_2(\mu\text{-}O_2CAr^{Tol})_4\}$ paddlewheel [158]. Each iron center is square pyramidal with the *N*-donor occupying the apical position. The markedly contracted Fe···Fe distance of 2.8222(8) Å matches closely with those of other tetrabridged structures such as **38**. In analogy to **34**, a solution of $[Fe_2(\mu\text{-}O_2CAr^{Tol})_4(4\text{-}t\text{-}BuC_5H_4N)_2]$ (**39**) in CH_2Cl_2 reacts with O_2 at -78°C to yield a deep green intermediate **40**. This product(s) appears to be equivalent spectroscopically to **37** (vide infra), a result that suggests the $Ar^{Tol}CO_2^-$ groups might be capable of undergoing carboxylate shifts. Although no direct proof is available for repositioning of the carboxylates during the oxygenation reaction, the bis-carboxylate bridged diiron(III) adduct, $[Fe_2(O_2CAr^{Tol})_2(\mu\text{-}O_2CAr^{Tol})_2(\mu\text{-}OH)_2(4\text{-}t\text{-}BuC_5H_4N)_2]$ (**41**), can be isolated in $\sim 90\%$ yield following thermolysis. Metrical parameters for **41** are comparable to those of **38**.

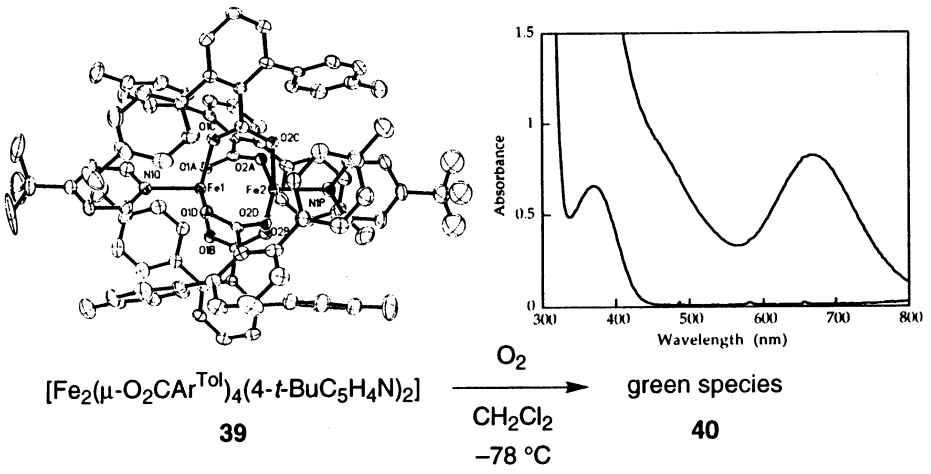

Scheme 6.

UV–vis spectroscopy indicates that the green species generated from **39** is analogous to that formed with **34** [158]. Low temperature oxygenation of a dilute CH_2Cl_2 solution of **39** results in the development of a broad CT absorption centered at ~ 670 nm. Slow bleaching of this band is observed when **40** is titrated with a solution of $[(Cp^*)_2Fe]$; an optical transition appears at 780 nm due to the formation of $[(Cp^*)_2Fe]^+$. After addition of 0.4–0.5 equivalents of $[(Cp^*)_2Fe]$, the 670 nm band is extinguished completely. The green product does not appear to be a powerful enough oxidant to react with $[Cp_2Fe]$. These findings allow an upper and lower limit for the reduction potential of **40** to be set between 0.46 and -0.13 V (vs. SCE). Reactions of substituted phenols with **40** demonstrate further the oxidizing ability of a species present in the solution of **40**. Treatment with two equivalents of 2,4-di-*t*-butylphenol affords the coupled product 3,3′,5,5′-tetra-*t*-butyl-1,1′-biphenol in 40% yield (reaction stoichiometry based on **39**; yield assumes **40** is a one-electron oxidant). This result demonstrates that some fraction of the solution produced upon oxygenation of **39** is oxidized above the Fe^{3+}/Fe^{3+} level, a conclusion that has been verified by EPR spectroscopy. The spectrum of **40** shows a strong isotropic $g = 2.00$ ($S = 1/2$) signal and a less intense feature at $g = 9.66$ ($S = 9/2$). Based on these and additional EPR data, the sample of **40** is believed to contain mixed-valence Fe^{3+}/Fe^{4+} species that constitute $\sim 40\%$ of the bulk material.

Mössbauer spectra on a solid sample of **40** can be deconvoluted into three major components [158]. A portion of the material ($\sim 30\%$ of the total iron) has been assigned to an antiferromagetically coupled diiron(III) species based on the observation of a central quadrupole doublet with $\delta = 0.54$ mm s^{-1} and $\Delta E_Q = 1.13$ mm s^{-1}. A magnetically-split Mössbauer spectrum shows well-resolved peaks at -3.8, -1.7, 2.0, and 4.9 mm s^{-1} that arise from the $S = 1/2$ product. From these data, it is possible to quantitate the $S = 1/2$ material as representing $\sim 36\%$ of the total

iron in the sample. Only this species is expected to have a strong dependence on the orientation of the applied magnetic field with respect to the direction of the γ-rays. Consequently, δ and ΔE_Q values for the $S = 1/2$ derivative can be extracted from the difference plot of two spectra recorded at parallel and perpendicular applied magnetic fields. The observed isomer shifts of $\delta_1 = 0.55$ mm s^{-1} and $\delta_2 = 0.12$ mm s^{-1} provide compelling evidence that the $S = 1/2$ component is a mixed-valence Fe(III)/Fe(IV) species. This product represents the first example of an Fe(IV) complex that has been prepared by reaction of dioxygen with an Fe(II) starting material, a process that closely mimics the chemistry of certain diiron metalloenzymes. The third species, the green component, has been identified as the mixed-valence Fe(II)Fe(III) one-electron oxidation product of **39**.

The reaction chemistry of $[Fe_2(\mu\text{-}O_2CAr^{Mes})_2(O_2CAr^{Mes})_2(CH_3CN)_2]$ (**36**) with dioxygen is different from that of **39** [157]. Addition of O_2 to a CH_2Cl_2 solution of **36** at -50°C generates immediately and irreversibly an EPR silent purple species **42** ($\lambda_{max} = 540$ nm, $\varepsilon = 2300$ M^{-1} cm^{-1}). At this temperature **42** is stable for >12 h and only slowly decomposes upon warming to 25°C ($t_{1/2} \sim 30$ h), ultimately furnishing a brown solution (Eq. (7)). The interesting stability of **42** derives unquestionably from the extreme steric hindrance around the metal centers provided by the mesityl groups. This purple product has been assigned as a diferric 1,2-peroxide based on UV–vis and rR spectroscopy. Excitation of **42** into the putative peroxo O–Fe^{3+} LMCT transition results in a resonance enhanced band at 885 cm^{-1}, which shifts to 871 cm^{-1} upon incorporation of $^{18}O_2$. No other isotope-sensitive bands are observed.

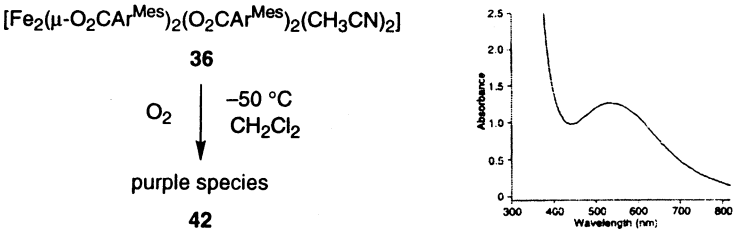

(7)

The assignment of the 885-cm^{-1} vibration as an O–O stretch is consistent with other known $Fe_2(O_2)$ constructs. The isotope shift of 14 cm^{-1}, however, is much smaller than expected for an uncoupled harmonic oscillator. Additional investigations of this system are warranted to characterize both the purple species **42** and the product(s) of its decomposition.

3.2.5. H_2Ph_4DBA

Unlike each of the systems discussed previously, the dicarboxylate ligand H_2Ph_4DBA was designed specifically to model the structure and function of the dioxygen-binding protein hemerythrin (Hr) [160]. A key design criterion was to reproduce more faithfully than in XDK derivatives the nearly perpendicular orientation of the two carboxylate groups that bridge both iron centers in the active site of Hr. Computer modeling suggested that the structure of dibenzofuran-4,6-di-

acetic acid (H_2DBA) would present an orthogonal pair of properly spaced carboxylate ligands. The basic framework of H_2DBA was further elaborated by replacing all four benzylic methylene hydrogens with phenyl groups to afford dibenzofuran-4,6-bis(diphenylacetic acid) (**43**) (H_2Ph_4DBA). The incorporation of these bulky aromatic units was expected to preorganize the two carboxylates in an appropriate conformation for bridging two metal centers. Moreover, it was hoped that these groups would promote both crystallinity as well as solubility of the resulting diiron adducts.

The intrinsic ability of Ph_4DBA to chelate two metal ions is demonstrated in the efficient synthesis of (μ-hydroxo)bis(μ-carboxylato)diiron(II) complexes, obtained through self-assembly reactions using $Fe(OTf)_2{\cdot}(CH_3CN)_2$ as a ferrous ion source (Fig. 15). Terminal capping ligands serve a critical role in stabilizing these dinuclear structures. Specifically, the use of the bidentate chelate *N*,*N*,*N*′,*N*′-tetramethylethylenediamine (TMEDA) affords the neutral compound [Fe_2(μ-OH)(μ-Ph_4DBA)(TMEDA)$_2$(OTf)] (**44**), in which one iron site is six-coordinate (Fe1) and the other is coordinatively unsaturated (Fe2). Complex **44** represents the first model compound to reproduce in the solid-state the asymmetric coordination environment of deoxyHr. The terminal sites on the (μ-hydroxo) bis(μ-carboxylate) diiron(II) core of **44** are filled by two TMEDA ligands and one triflate counterion. The difference in coordination numbers of Fe1 and Fe2 is reflected in the systematically longer metal–ligand bond lengths at the coordinatively saturated Fe1 center. An Fe···Fe separation of 3.26 Å and 111° Fe–O(H)–Fe bond angle in **44** compare favorably to those values reported for deoxyHr (3.32 Å and 111°, respectively). The bis(μ-carboxylate) coordination mode of Ph_4DBA^{2-} forces the plane of the dibenzofuran unit to cant towards one of the metal centers (Fe1). The chemical inequivalence between metal sites in Ph_4DBA-bridged complexes may be attributed in part to this structural feature.

Mössbauer spectroscopy on a powdered sample of **44** (77 K) shows a broad, symmetric doublet. The parameters obtained by fitting the data to a single quadrupole doublet are virtually identical to those of deoxyHr ($\delta = 1.19$ mm s^{-1}, $\Delta E_Q = 2.81$ mm s^{-1}) and indicative of high-spin iron(II). Although the quality of the fit is reasonable, the breadth of the lines ($\Gamma \approx 0.70$ mm s^{-1}) suggests that this

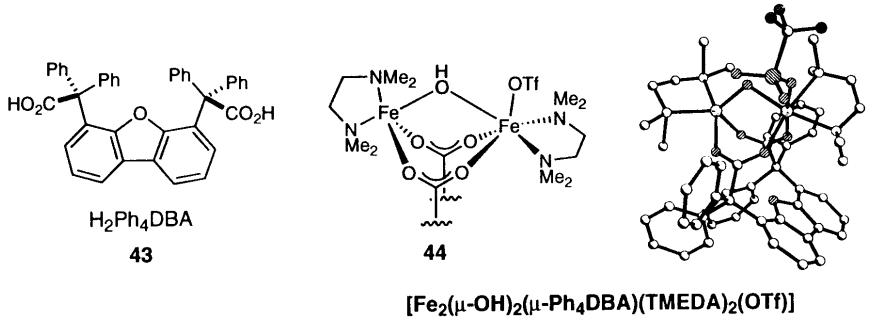

Fig. 15. Hemerythrin model complex derived from H_2Ph_4DBA.

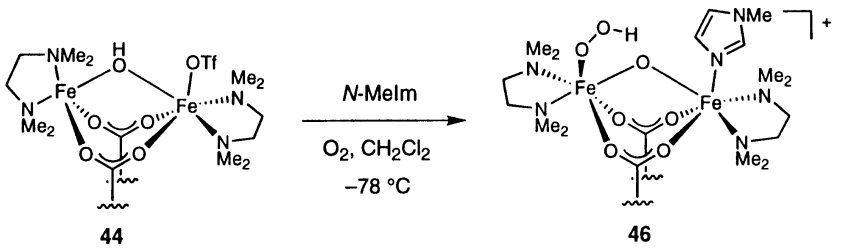

44 46

Scheme 7.

spectrum may be composed of two overlapping quadrupole doublets ($\delta_1 = 1.04$ mm s^{-1}, $\Delta E_{Q1} = 2.81$ mm s^{-1}; $\delta_2 = 1.33$ mm s^{-1}, $\Delta E_{Q2} = 2.81$ mm s^{-1}). This interpretation is consistent with the crystallographically observed asymmetry in the coordination structures of the two iron sites in **44**. The Mössbauer spectrum of a frozen THF solution of **44** containing three equivalents of *N*-MeIm, however, shows a relatively sharp doublet ($\Gamma \approx 0.35$ mm s^{-1}) with $\delta = 1.23$ mm s^{-1} and $\Delta E_Q = 2.85$ mm s^{-1}. Accordingly, the spectral differences between the solid and frozen solution samples indicate that a structural change within the diiron unit occurs upon dissolution, possibly resulting from displacement of the triflate (TfO^-) anion by *N*-MeIm. Conductivity experiments in EtCN at 25°C show electrolytic behavior and, thereby, support the proposal for TfO^- dissociation. In addition, metathesis of **44** in CH_3CN using sodium tetraphenylborate ($NaBPh_4$) results in substitution of the TfO^- ligand for a solvent molecule, as shown by X-ray analysis. The structure of $[Fe_2(\mu\text{-OH})(\mu\text{-Ph}_4\text{DBA})(\text{TMEDA})_2(CH_3CN)]^+$ (**45**) reveals that the asymmetric coordination environment of the iron centers is preserved in this cationic diferrous complex.

Conditions have been found to generate an analog of oxyHr from **44** by direct reaction with dioxygen. When O_2 is bubbled through a solution of this compound in CH_2Cl_2 containing three equivalents of *N*-MeIm at -78°C, the initially colorless solution rapidly and irreversibly turns red-orange (Scheme 7). The absorption spectrum of the colored species **46** displays maxima at 336 and 470 nm with extinction coefficients of 7300 and 2600 M^{-1} cm^{-1}, respectively. Comparison of this spectrum with that of oxyHr ($\lambda_{max} = 330$, 500 nm; $\varepsilon = 6800$, 2200 M^{-1} cm^{-1}) shows remarkable similarities in overall shape, position, and intensity of the absorption profiles [25]. A distinguishing feature in the spectrum of oxyHr is the relatively intense 500-nm band arising from hydroperoxide O–Fe^{3+} LMCT transitions. By direct analogy, the 470-nm band in the oxygenated model system may be assigned to the same set of transitions, and implicates strongly the presence of a hydroperoxide ligand bound terminally to a ferric center. The position of this band argues against the formation of a (μ-1,2-peroxo)diiron(III) complex for which the visible CT band would be expected to maximize at a wavelength ≥ 600 nm. Low-temperature oxygenation of **44** in the absence of *N*-MeIm is also accompanied by absorption changes indicative of metal-centered oxidation, but does not afford an oxyHr-like UV–vis spectrum. *N*-MeIm can be substituted with *N*-benzylimida-

zole, but neither *N*-methylbenzimidazole nor pyridine effects hydroperoxide generation. Presumably, only small *N*-donors can access the sterically encumbered Fe1 site.

Direct evidence for the presence of an O–O unit in the red-orange adduct is obtained from rR spectroscopy. Laser excitation into the putative hydroperoxide O–Fe^{3+} CT band yields a resonance-enhanced feature at 844 cm^{-1} indicative of a metal-bound peroxide. The assignment of this rR band to an O–O stretch was confirmed by using $^{18}O_2$ which gives a $\nu(^{18}O–^{18}O) = 798$ cm^{-1}. The magnitude of this shift is consistent with an uncoupled harmonic oscillator. These frequencies are identical to those observed in oxyHr (844 cm^{-1} for $^{16}O_2$) [24]. Mössbauer data on the reaction product of **44** and O_2 also supports the formulation of **46** as an iron(III) peroxide species. The spectrum of an oxygenated sample in THF (77 K) containing three equivalents of *N*-MeIm shows a pair of lines that cannot be fit adequately to a single quadrupole doublet. Two overlapping signals of similar integrated intensity, however, afford a reasonable simulation ($\delta_1 = 0.51$ mm s^{-1}, $\Delta E_{Q1} = 1.08$ mm s^{-1}; $\delta_2 = 0.50$ mm s^{-1}, $\Delta E_{Q2} = 1.70$ mm s^{-1}). These parameters compare favorably with those used to fit the spectrum of oxyHr ($\delta_1 = 0.48$ mm s^{-1}, $\Delta E_{Q1} = 1.03$ mm s^{-1}; $\delta_2 = 0.51$ mm s^{-1}, $\Delta E_{Q2} = 1.93$ mm s^{-1}), and suggest that the conversion of **44** to the red-orange adduct **46** generates two distinct high-spin iron(III) sites [161]. Such findings are consistent with a model in which a hydroperoxide is bound terminally to a single ferric center. In addition, the magnitude of ΔE_{Q1} and ΔE_{Q2} attests to the presence of a μ-oxo group linking two distinct iron sites. Recent EPR spectroscopic studies on a cryoreduced sample of the hydroperoxide-bound adduct validate the assignment of **46** as a (μ-oxo)diiron(III) hydroperoxide [160].

The assembly of **46** is believed to occur via reaction of O_2 at the five-coordinate ferrous center (Fe2) in $[Fe_2(\mu\text{-OH})(\mu\text{-Ph}_4\text{DBA})(\text{TMEDA})_2(N\text{-MeIm})]^+$ (**47**). The existence of a hydrogen bond between the terminal hydroperoxide ligand and the oxide bridge in **46** remains to be established. The thermally unstable nature of **46** has precluded the use of X-ray crystallography to determine unequivocally its geometric structure. Even at reduced temperatures (-78°C), the characteristic visible absorption band of **46** bleaches over the course of hours, as marked by the slow disappearance of the $\{Fe(O_2H)\}^{2+}$ chromophore. Thermal decomposition of this complex in CH_2Cl_2–THF yields solid material that can be recrystallized to furnish dark red single crystals. X-ray analysis of this compound reveals a novel tetranuclear ferric cluster, $[Fe_4(\mu_3\text{-O})(\mu\text{-O})(\mu\text{-OH})_2(\mu\text{-Ph}_4\text{DBA})_2(\text{TMEDA})_3]^{2+}$ (**48**), in which portions from two molecules of the diferrous starting material **44** are readily apparent. This dioxygen-dependent dimerization process requires dissociation of one TMEDA ligand and a positional shift by one carboxylate group from a μ-1,3 to a terminal, bidentate mode [161]. Avoiding the decomposition pathway that leads to structures such as **48** through rational ligand modification represents the next step towards the development of a stable hydroperoxide model system capable of binding dioxygen reversibly.

4. Conclusions

We have presented within the context of this review some of the most advanced diiron model systems prepared to date. Collectively, this work has provided insight into the reaction chemistry of ferrous ion and dioxygen with molecular detail that is difficult to obtain through studies on biomolecules. Investigations have focused principally on controlling the initial reduction of O_2 to the peroxide level. Three diferric peroxides, each possessing different stabilities and unique reactivities, have been characterized crystallographically. One system, $[Fe_2(O_2)(O_2CBn)_2(HB(3,5\text{-}^iPr_2pz)_3)_2]$ (**4**), is believed to model closely an early observable intermediate (H_{peroxo}) in the sMMO reaction cycle as well as the analogous peroxide species characterized in Δ^9D and a mutant of R2. Through X-ray and spectroscopic analyses of **4** and $[Fe_2(O_2)(OBz)_2(HB(3,5\text{-}^iPr_2pz)_3)_2]$ (**2**), an electronic structural description has been formulated for O_2^{2-} bonding in diiron compounds. The results from these investigations suggest that proton activation, either by H^+ transfer or H-bonding, of the O–O unit may be required to trigger its subsequent conversion to a reactive, electrophilic oxidant. Reactivity studies with **2** and XDK-based $Fe_2^{III}(O_2)$ adducts, which demonstrate that the O_2^{2-} ligand is basic in nature, offer support for this conclusion. In this regard, the chemistry of XDK peroxide compounds may be the most revealing given the exactness of the ligand composition to that of the protein metallocofactor.

A recent finding that H_{peroxo} in MMOH is capable of epoxidizing unfunctionalized alkenes offers compelling evidence for a peroxide with electrophilic character [84]. How can the discrepancy between the small-molecule and protein peroxide reactivity be resolved? The apparent difference may be tied to the presence of a cysteine (Cys-151) and a threonine (Thr-213) in the active site of MMOH. Either of these residues located proximally to the diiron cluster could protonate the O_2^{2-} group in H_{peroxo} thereby generating a hydroperoxide. Alternatively, an iron-bound H_2O molecule might function as a proton or H-bonding source. Numerous illustrations of *O*-atom transfer to alkenes by metal-bound hydroperoxide species, including recent examples with mononuclear ferric hydroperoxides, have been documented [162–164]. It is possible that protonation activates H_{peroxo} as an epoxidizing agent in a step that is not rate-limiting and, therefore, not kinetically observable. At this time, no studies on small-molecule, diferric peroxide systems have been described that explore proton-coupled substrate oxidation. Testing these ideas experimentally requires the generation of peroxide adducts that demonstrate increased thermal stability together with ligands that do not dissociate readily in the presence of H^+ donors.

What conclusions can be drawn about the current mechanistic model for substrate oxidation in non-heme metalloenzymes? Available data from biochemical and synthetic studies strongly support the intermediacy of a diferric peroxide on the reaction coordinate. The half-life of this species differs among the various enzymes. Factors responsible for controlling the peroxide stability from one protein system to another remain unclear. In sMMO, it is generally accepted that H_{peroxo} transforms to a high valent iron species prior to alkane oxidation. Mössbauer and EXAFS data

bolster claims that this intermediate, **Q**, contains two Fe^{4+} centers and has a short metal-metal distance (ca. 2.5 Å) [85,101,102]. Due to the paucity of available structural data on **Q** and the absence of a model compound that mimics its reactivity and signature UV–vis spectrum, the details of H_{peroxo} to **Q** conversion are left to theory and speculation. An equally obscure facet of the mechanism centers on the oxidation event(s) that converts alkane to alcohol. Most indications are that the reaction of substrate with **Q** (irrespective of its form) does not pass through a discrete radical intermediate. Certain computational models favor concerted or asynchronous-concerted transition states that involve direct *O*-atom insertion into a C–H bond. Other theoretical constructs predict the intermediacy of iron-alkane σ-adducts and/or organometallic species prior to C–O bond formation. The next generation of synthetic model compounds should begin to unravel some of these questions, the mysteries that shroud intermediate **Q** and its putative function as an oxidant. To accomplish this task, systems that incorporate features present in the second and third shells of the protein active site (e.g. cysteine and threonine residues, hydrophobic contacts, hydrogen bonds) may be required. Ligand scaffolds must isolate reactive metal centers and oxygenated intermediates to block bimolecular decomposition pathways and the initiation of autoxidation reactions. These structures must also possess enough flexibility for groups to reposition and for metal ions to alter coordination numbers and geometries throughout a reaction cycle. Finally, one needs to consider the capacity of the protein pocket to hold substrate within close contact of the reactive oxidant, thus establishing a high effective reactant molarity. Consolidating each of these concepts into a single model complex poses formidable challenges in ligand architecture and construction. Given all of the complexities associated with molecular design, synthesis, and the regulation of reactivity, the modeling of non-heme diiron metalloenzymes should remain an area rich with opportunities for discovery for some time to come.

Acknowledgements

This work was supported by grants from the National Institute of General Medical Sciences and the National Science Foundation. J.D.B. and T.J.M. thank the National Institutes of Health for Postdoctoral Fellowships.

References

[1] R.H. Holm, P. Kennepohl, E.I. Solomon, Chem. Rev. 96 (1996) 2239.
[2] J.S. Valentine, T.V. O'Halloran, Curr. Opin. Chem. Biol. 3 (1999) 129.
[3] A.L. Feig, S.J. Lippard, Chem. Rev. 94 (1994) 759.
[4] P. Nordlund, H. Eklund, Curr. Opin. Struct. Biol. 5 (1995) 758.
[5] B.J. Wallar, J.D. Lipscomb, Chem. Rev. 96 (1996) 2625.
[6] D.M. Kurtz Jr, J. Biol. Inorg. Chem. 2 (1997) 159.
[7] S.J. Lange, L. Que Jr, Curr. Opin. Chem. Biol. 2 (1998) 159.

[8] D.H.R. Barton, A.E. Martell, D.T. Sawyer (Eds.), The Activation of Dioxygen and Homogeneous Catalytic Oxidation, Plenum, New York, 1993.
[9] R.A. Sheldon, J.K. Kochi, Metal-Catalyzed Oxidations of Organic Compounds, Academic Press, New York, 1981.
[10] H.C. Liang, M. Dahan, K.D. Karlin, Curr. Opin. Chem. Biol. 3 (1999) 168.
[11] H.F. Hsu, Y.H. Dong, L.J. Shu, V.G. Young Jr, L. Que Jr, J. Am. Chem. Soc. 121 (1999) 5230.
[12] C. Kim, Y. Dong, L. Que Jr, J. Am. Chem. Soc. 119 (1997) 3635.
[13] S. Ménage, B.A. Brennan, C. Juarez-Garcia, E. Münck, L. Que Jr, J. Am. Chem. Soc. 112 (1990) 6423.
[14] M. Fontecave, S. Ménage, C. Duboc-Toia, Coord. Chem. Rev. 178 (1998) 1555.
[15] L. Que Jr., J. Chem. Soc. Dalton Trans. (1997) 3933.
[16] L. Que Jr, Y. Dong, Acc. Chem. Res. 29 (1996) 190.
[17] R.G. Wilkins, Chem. Soc. Rev. (1992) 171.
[18] D.M. Kurtz Jr, D.F. Shriver, I.M. Klotz, Coord. Chem. Rev. 24 (1997) 145.
[19] R.E. Stenkamp, Chem. Rev. 94 (1994) 715.
[20] P.C. Wilkins, R.G. Wilkins, Coord. Chem. Rev. 79 (1987) 195.
[21] M.A. Holmes, I. Le Trong, S. Turley, L.C. Sieker, R.E. Stenkamp, J. Mol. Biol. 218 (1991) 583.
[22] M.A. Holmes, R.E. Stenkamp, J. Mol. Biol. 220 (1991) 723.
[23] J.-H. Zhang, D.M. Kurtz Jr, Y.-M. Xia, P.G. Debrunner, Biochim. Biophys. Acta 1122 (1992) 293.
[24] A.K. Shiemke, T.M. Loehr, J. Sanders-Loehr, J. Am. Chem. Soc. 106 (1984) 4951.
[25] R.C. Reem, J.M. McCormick, D.E. Richardson, F.J. Devlin, P.J. Stephens, R.L. Musselman, E.I. Solomon, J. Am. Chem. Soc. 111 (1989) 4688.
[26] S. Pulver, W.A. Froland, B.G. Fox, J.D. Lipscomb, E.I. Solomon, J. Am. Chem. Soc. 115 (1993) 12409.
[27] J.B.R. Dunn, A.W. Addison, R.E. Bruce, J. Sanders-Loehr, T.M. Loehr, Biochemistry 16 (1977) 1743.
[28] H. Thomann, M. Bernardo, J.M. McCormick, S. Pulver, K.K. Andersson, J.D. Lipscomb, E.I. Solomon, J. Am. Chem. Soc. 115 (1993) 8881.
[29] J.M. McCormick, R.C. Reem, E.I. Solomon, J. Am. Chem. Soc. 113 (1991) 9066.
[30] A. Jordan, P. Reichard, Ann. Rev. Biochem. 67 (1998) 71.
[31] J. Stubbe, P. Riggs-Gelasco, Trends Biochem. Sci. 23 (1998) 438.
[32] B.-M. Sjöberg, in: F. Eckstein, D. Lilley Jr (Eds.), Nucleic Acids and Molecular Biology, vol. 9, Springer, Germany, 1995, pp. 192–221.
[33] J. Stubbe, W.A. van der Donk, Chem. Biol. 2 (1995) 793.
[34] M. Eriksson, A. Jordan, H. Eklund, Biochemistry 37 (1998) 13359.
[35] J. Stubbe, W. van der Donk, Chem. Rev. 98 (1998) 705.
[36] N. Ravi, J.M. Bollinger Jr, B.H. Huynh, D.E. Edmondson, J. Stubbe, J. Am. Chem. Soc. 116 (1994) 8007.
[37] J.M. Bollinger Jr, W.H. Tong, N. Ravi, B.H. Huynh, D.E. Edmondson, J. Stubbe, J. Am. Chem. Soc. 116 (1994) 8015.
[38] J.M. Bollinger Jr, W.H. Tong, N. Ravi, B.H. Huynh, D.E. Edmondson, J. Stubbe, J. Am. Chem. Soc. 116 (1994) 8024.
[39] D.T. Logan, F.d. Maré, B.O. Persson, A. Slaby, B.-M. Sjöberg, P. Nordlund, Biochemistry 37 (1998) 10798.
[40] A.M. Valentine, S.J. Lippard, J. Chem. Soc. Dalton (1997) 3925.
[41] H. Dalton, P. Wilkins, Biochem. Soc. Trans. 25 (1997) 69.
[42] K.E. Liu, S.J. Lippard, in: A.G. Sykes (Ed.), Advances in Inorganic Chemistry, vol. 42, Academic Press, San Diego, CA, 1995, pp. 263–289.
[43] A.K. Nielsen, K. Gerdes, J.C. Murrell, Mol. Microbiol. 25 (1997) 399.
[44] A.K. Nielsen, K. Gerdes, H. Degn, J.C. Murrell, Microbiology 142 (1996) 1289.
[45] H.-H.A.T. Nguyen, M. Zhu, S.J. Elliott, K.H. Nakagawa, B. Hedman, A.M. Costello, T.L. Peeples, B. Wilkinson, H. Morimoto, P.G. Williams, H.G. Floss, M.E. Lidstrom, K.O. Hodgson, S.I. Chan, in: M.E. Lidstrom, F.R. Tabita (Eds.), Microbial Growth on C1 Compounds, Kluwer, Dordrecht, The Netherlands, 1996, pp. 150–158.

[46] G.T. Gassner, D.A. Kopp, J.L. Blazyk, S.J. Lippard, J. Inorg. Biochem. 74 (1999) 136.
[47] R. Davydov, A.M. Valentine, S. Komar-Panicucci, B.M. Hoffman, S.J. Lippard, Biochemistry 38 (1999) 4188–4197.
[48] S.J. Lippard, in: D.P. Kessisoglou (Ed.), Bioinorganic Chemistry: An Inorganic Perspective of Life, Kluwer, Dordrecht, The Netherlands, 1995, pp. 1–12.
[49] K.E. Liu, A.L. Feig, D.P. Goldberg, S.P. Watton, S.J. Lippard, in: D.H.R. Barton, A.E. Martell, D.T. Sawyer (Eds.), Fifth International Symposium on the Activation of Dioxygen and Homogeneous Catalytic Oxidation, Plenum, New York, 1993, pp. 301–320.
[50] A.C. Rosenzweig, H. Brandstetter, D.A. Whittington, P. Nordlund, S.J. Lippard, C.A. Frederick, Proteins 29 (1997) 141.
[51] A.C. Rosenzweig, S.J. Lippard, Acc. Chem. Res. 27 (1994) 229.
[52] A.C. Rosenzweig, P. Nordlund, P.M. Takahara, C.A. Frederick, S.J. Lippard, Chem. Biol. 2 (1995) 409.
[53] S.-K. Lee, J.D. Lipscomb, Biochemistry 38 (1999) 4423.
[54] A.D.N. Vaz, D.F. McGinnity, M.J. Coon, Proc. Natl. Acad. Sci. USA 95 (1998) 3555.
[55] A.C. Rosenzweig, C.A. Frederick, S.J. Lippard, P. Nordlund, Nature 366 (1993) 537.
[56] P. Nordlund, H. Eklund, J. Mol. Biol. 232 (1993) 123.
[57] P. Nordlund, B.-M. Sjöberg, H. Eklund, Nature 345 (1990) 593.
[58] J. Shanklin, E.B. Cahoon, Ann. Rev. Plant Physiol. Plant Mol. Biol. 49 (1998) 611.
[59] P. Broun, J. Shanklin, E. Whittle, C. Somerville, Science (1998) 282.
[60] J.A. Broadwater, J.A. Haas, B.G. Fox, FETT-Lipid 100 (1998) 103.
[61] J. Ai, J.A. Broadwater, T.M. Loehr, J. Sanders-Loehr, B.G. Fox, J. Biol. Inorg. Chem. 2 (1997) 37.
[62] Y. Lindqvist, W. Huang, G. Schneider, J. Shanklin, EMBOJ. 15 (1996) 4081.
[63] B.G. Fox, J. Shanklin, J. Ai, T.M. Loehr, J. Sanders-Loehr, Biochemistry 33 (1994) 12776.
[64] B.G. Fox, J. Shanklin, C. Somerville, E. Münck, Proc. Natl. Acad. Sci. USA 90 (1993) 2486.
[65] L.J. Shu, J.A. Broadwater, C. Achim, B.G. Fox, E. Munck, L. Que Jr, J. Biol. Inorg. Chem. 3 (1998) 392.
[66] Y.-S. Yang, J.A. Broadwater, S.C. Pulver, B.G. Fox, E.I. Solomon, J. Am. Chem. Soc. 121 (1999) 2770.
[67] J.A. Broadwater, J. Ai, T.M. Loehr, J. Sanders-Loehr, B.G. Fox, Biochemistry 37 (1998) 14664.
[68] E.B. Cahoon, Y. Lindqvist, G. Schneider, J. Shanklin, Proc. Natl. Acad. Sci. USA 94 (1997) 4872–4877.
[69] W.H. Tong, S. Chen, S.G. Lloyd, D.E. Edmondson, B.H. Huynh, J. Stubbe, J. Am. Chem. Soc. 118 (1996) 2107.
[70] J.D. Pikus, J.M. Studts, K. McClay, R.J. Steffan, B.G. Fox, Biochemistry 36 (1997) 9283.
[71] L.M. Newman, L.P. Wackett, Biochemistry 34 (1995) 14066.
[72] J.D. Pikus, K.H. Mitchell, K. McClay, R.J. Steffan, B.G. Fox, J. Inorg. Biochem. 74 (1999) 236.
[73] J.D. Pikus, J.M. Studts, C. Achim, K.E. Kauffmann, E. Münck, R.J. Steffan, K. McClay, B.G. Fox, Biochemistry 35 (1996) 9106.
[74] N.Y. Zhou, A. Jenkins, C.K.N.C.K. Chion, D.J. Leak, Appl. Environ. Microbiol. 65 (1999) 1589.
[75] S.C. Gallagher, A. George, H. Dalton, Eur. J. Biochem. 254 (1998) 480.
[76] A.N. Onumonu, A. Colocoussi, C. Matthews, M.P. Woodland, D.J. Leak, Biocatalysis 10 (1994) 211.
[77] N.Y. Zhou, A. Jenkins, C.K.N.C.K. Chion, D.J. Leak, FEBS Lett. 430 (1998) 181.
[78] F.J. Small, S.A. Ensign, J. Biol. Chem. 272 (1997) 24913.
[79] S.C. Gallagher, R. Cammack, H. Dalton, Eur. J. Biochem. 247 (1997) 635.
[80] J. Shanklin, C. Achim, H. Schmidt, B.G. Fox, E. Münck, Proc. Natl. Acad. Sci. USA 94 (1997) 2981.
[81] J. Peters, B. Witholt, Biochim. Biophys. Acta-Biomembr. 1196 (1994) 145.
[82] H.F. Hsu, L. Que Jr, J. Shanklin, J. Inorg. Biochem. 74 (1999) 168.
[83] J. Shanklin, E. Whittle, B.G. Fox, Biochemistry 33 (1994) 12787.
[84] A.M. Valentine, S.S. Stahl, S.J. Lippard, J. Am. Chem. Soc. 121 (1999) 3876.

[85] K.E. Liu, A.M. Valentine, D. Wang, B.H. Huynh, D.E. Edmondson, A. Salifoglou, S.J. Lippard, J. Am. Chem. Soc. 117 (1995) 10174.
[86] K.E. Liu, A.M. Valentine, D. Qiu, D.E. Edmondson, E.H. Appelman, T.G. Spiro, S.J. Lippard, J. Am. Chem. Soc. 117 (1995) 4997.
[87] S.-K. Lee, J.C. Nesheim, J.D. Lipscomb, J. Biol. Chem. 268 (1993) 21569.
[88] D.D. LeCloux, A.M. Barrios, T.J. Mizoguchi, S.J. Lippard, J. Am. Chem. Soc. 120 (1998) 9001.
[89] K. Kim, S.J. Lippard, J. Am. Chem. Soc. 118 (1996) 4914.
[90] K.E. Liu, D. Wang, B.H. Huynh, D.E. Edmondson, A. Salifoglou, S.J. Lippard, J. Am. Chem. Soc. 116 (1994) 7465.
[91] Y. Liu, J.C. Nesheim, S.-K. Lee, J.D. Lipscomb, J. Biol. Chem. 270 (1995) 24662.
[92] S.E. Parkin, S. Chen, B.A. Ley, L. Mangravite, D.E. Edmonson, B.H. Huynh, J.M. Bollinger Jr, Biochemistry 37 (1998) 1124.
[93] M. Ormö, F. deMaré, K. Regnström, A. Åberg, M. Sahlin, J. Ling, T.M. Loehr, J. Sanders-Loehr, B.-M. Sjöberg, J. Biol. Chem. 267 (1992) 8711.
[94] J.M. Bollinger Jr, C. Krebs, A. Vicol, S. Chen, B.A. Ley, D.E. Edmondson, B.H. Huynh, J. Am. Chem. Soc. 120 (1998) 1094.
[95] P. Moënne-Loccoz, J. Baldwin, B.A. Ley, T.M. Loehr, J.M. Bollinger Jr, Biochemistry 37 (1998) 14659.
[96] T.C. Brunold, N. Tamura, N. Kitajima, Y. Moro-oka, E.I. Solomon, J. Am. Chem. Soc. 120 (1998) 5674.
[97] D.E. Edmondson, B.H. Huynh, Inorg. Chim. Acta 252 (1996) 399.
[98] J.-P. Willems, H.-I. Lee, D. Burdi, P.E. Doan, J. Stubbe, B.M. Hoffman, J. Am. Chem. Soc. 119 (1997) 9816.
[99] B.E. Sturgeon, D. Burdi, S. Chen, B.H. Huynh, D.E. Edmondson, J. Stubbe, B.M. Hoffman, J. Am. Chem. Soc. 118 (1996) 7551.
[100] P. Riggs-Gelasco, L. Shu, S. Chen, D. Burdi, B.H. Huynh, L. Que Jr, J. Stubbe, J. Am. Chem. Soc. 120 (1998) 849.
[101] S.-K. Lee, B.G. Fox, W.A. Froland, J.D. Lipscomb, E. Münck, J. Am. Chem. Soc. 115 (1993) 6450.
[102] L. Shu, J.C. Nesheim, K. Kauffmann, E. Münck, J.D. Lipscomb, L. Que Jr, Science 275 (1997) 515.
[103] P.E.M. Siegbahn, R.H. Crabtree, P. Nordlund, J. Biol. Inorg. Chem. 3 (1998) 314.
[104] P.E.M. Siegbahn, R.H. Crabtree, J. Am. Chem. Soc. 119 (1997) 3103.
[105] A.M. Valentine, M.H. LeTadic-Biadatti, P.H. Toy, M. Newcomb, S.J. Lippard, J. Biol. Chem. 274 (1999) 10771.
[106] A.M. Valentine, B. Wilkinson, K.E. Liu, S. Komar-Panicucci, N.D. Priestley, P.G. Williams, H. Morimoto, H.G. Floss, S.J. Lippard, J. Am. Chem. Soc. 119 (1997) 1818.
[107] K.E. Liu, C.C. Johnson, M. Newcomb, S.J. Lippard, J. Am. Chem. Soc. 115 (1993) 939.
[108] S.-Y. Choi, P.E. Eaton, P.F. Hollenberg, K.E. Liu, S.J. Lippard, M. Newcomb, D.A. Putt, S.P. Upadhyaya, Y. Xiong, J. Am. Chem. Soc. 118 (1996) 6547.
[109] N.D. Priestley, H.G. Floss, W.A. Froland, J.D. Lipscomb, P.G. Williams, H. Morimoto, J. Am. Chem. Soc. 114 (1992) 7561.
[110] F. Ruzicka, D.-S. Huang, M.I. Donnelly, P.A. Frey, Biochemistry 29 (1990) 1696.
[111] D.H.R. Barton, Tetrahedron 54 (1998) 5805.
[112] D.H.R. Barton, Chem. Soc. Rev. 25 (1996) 237.
[113] R.J. Deeth, H. Dalton, J. Biol. Inorg. Chem. 3 (1998) 302.
[114] P.E.M. Siegbahn, Inorg. Chem. 38 (1999) 2880.
[115] B.D. Dunietz, M.D. Beachy, Y. Cao, D.A. Whittington, S.J. Lippard, R.A. Friesner, J. Am. Chem. Soc. 2000, in press.
[116] J.C. Nesheim, J.D. Lipscomb, Biochemistry 35 (1996) 10240.
[117] K. Yoshizawa, J. Biol. Inorg. Chem. 3 (1998) 318.
[118] K. Yoshizawa, T. Yamabe, R. Hoffmann, New J. Chem. 21 (1997) 151.
[119] K. Yoshizawa, Y. Shiota, T. Yamabe, Chem. Eur. J. 3 (1997) 1160.
[120] K. Yoshizawa, R. Hoffmann, Inorg. Chem. 35 (1996) 2409.

[121] K. Yoshizawa, T. Ohta, T. Yamabe, R. Hoffmann, J. Am. Chem. Soc. 119 (1997) 12311.
[122] K. Yoshizawa, A. Suzuki, T. Yamabe, J. Am. Chem. Soc. 121 (1999) 5266.
[123] A.F. Shestakov, A.E. Shilov, J. Mol. Catal. A: Chem. 105 (1996) 1.
[124] D.A. Whittington, A.M. Valentine, S.J. Lippard, J. Biol. Inorg. Chem. 3 (1998) 307.
[125] A.A. Shteinman, J. Biol. Inorg. Chem. 3 (1998) 325.
[126] J.D. Lipscomb, L. Que Jr, J. Biol. Inorg. Chem. 3 (1998) 331.
[127] K. Yoshizawa, T. Ohta, T. Yamabe, Bull. Chem. Soc. Jpn. 71 (1998) 1899.
[128] A. Rabion, S. Chen, J. Wang, R.M. Buchanan, J.-L. Seris, R.H. Fish, J. Am. Chem. Soc. 117 (1995) 12356.
[129] R.M. Buchanan, S. Chen, J.F. Richardson, M. Bressan, L. Forti, A. Morvillo, R.H. Fish, Inorg. Chem. 33 (1994) 3208.
[130] W.H. Armstrong, S.J. Lippard, J. Am. Chem. Soc. 105 (1983) 4837.
[131] K. Wieghardt, K. Pohl, W. Gebert, Angew. Chem. Int. Ed. Engl. 22 (1983) 727.
[132] T. Ookubo, H. Sugimoto, T. Nagayama, H. Masuda, T. Sato, K. Tanaka, Y. Maeda, H. Okawa, Y. Hayashi, A. Uehara, M. Suzuki, J. Am. Chem. Soc. 118 (1996) 701.
[133] Y. Dong, S. Yan, V.G. Young Jr, L. Que Jr, Angew. Chem. Int. Ed. Engl. 35 (1996) 618.
[134] D.M. Kurtz Jr, Chem. Rev. 90 (1990) 585.
[135] N. Kitajima, N. Tamura, H. Amagai, H. Fukui, Y. Moro-oka, Y. Mizutani, T. Kitagawa, R. Mathur, K. Heerwegh, C.A. Reed, C.R. Randall, L. Que Jr, K. Tatsumi, J. Am. Chem. Soc. 116 (1994) 9071.
[136] M.J. Baldwin, P.K. Ross, J.E. Pate, Z. Tyeklar, K.D. Karlin, E.I. Solomon, J. Am. Chem. Soc. 113 (1991) 8671.
[137] S. Mahapatra, J.A. Halfen, E.C. Wilkinson, G.F. Pan, X.D. Wang, V.G. Young, C.J. Cramer, L. Que Jr, W.B. Tolman, J. Am. Chem. Soc. 118 (1996) 11555.
[138] P.K. Ross, E.I. Solomon, J. Am. Chem. Soc. 113 (1991) 3246.
[139] S. Fox, K.D. Karlin, in: J.S. Valentine, C.S. Foote, A. Greenberg, J.F. Liebman (Eds.), Active Oxygen in Biochemistry, Blackie, Glasgow, 1995, pp. 188–231.
[140] M. Suzuki, Pure Appl. Chem. 70 (1998) 955.
[141] Y. Dong, S. Ménage, B.A. Brennan, T.E. Elgren, H.G. Jang, L.L. Pearce, L. Que Jr, J. Am. Chem. Soc. 115 (1993) 1851.
[142] H. Sugimoto, T. Nagayama, S. Maruyama, S. Fujinami, Y. Yasuda, M. Suzuki, A. Uehara, Bull. Chem. Soc. Jpn. 71 (1998) 2267.
[143] Y. Hayashi, T. Kayatani, H. Sugimoto, M. Suzuki, K. Inomata, A. Uehara, Y. Mizutani, T. Kitagawa, Y. Maeda, J. Am. Chem. Soc. 117 (1995) 11220.
[144] E. Kim, K.B. Lee, H.G. Jang, Bull. Chem. Soc. Korea 17 (1996) 1127.
[145] B.A. Brennan, Q. Chen, C. Juarez-Garcia, A.E. True, C.J. O'Connor, L. Que Jr, Inorg. Chem. 30 (1991) 1937.
[146] A.L. Feig, M. Becker, S. Schindler, R. van Eldik, S.J. Lippard, Inorg. Chem. 35 (1996) 2590.
[147] A.L. Feig, S.J. Lippard, J. Am. Chem. Soc. 116 (1994) 8410.
[148] S.P. Watton, A. Masschelein, J. Rebek Jr, S.J. Lippard, J. Am. Chem. Soc. 116 (1994) 5196.
[149] J.W. Yun, T. Tanase, S.J. Lippard, Inorg. Chem. 35 (1996) 7590.
[150] T.J. Mizoguchi, S.J. Lippard, Inorg. Chem. 36 (1997) 4526.
[151] S. Herold, L.E. Pence, S.J. Lippard, J. Am. Chem. Soc. 117 (1995) 6134.
[152] S. Herold, S.J. Lippard, J. Am. Chem. Soc. 119 (1997) 145.
[153] D.D. LeCloux, A.M. Barrios, S.J. Lippard, Bioorg. Med. Chem. 6 (1999) 1.
[154] C. Walling, Acc. Chem. Res. 31 (1998) 155.
[155] D.T. Sawyer, Coord. Chem. Rev. 165 (1997) 297.
[156] D. Lee, S.J. Lippard, J. Am. Chem. Soc. 120 (1998) 12153.
[157] J.R. Hagadorn, L. Que Jr, W.B. Tolman, J. Am. Chem. Soc. 120 (1998) 13531.
[158] D. Lee, J.D. Bois, D. Petasis, M.P. Hendrich, C. Krebs, B.H. Hyunh, S.J. Lippard, J. Am. Chem. Soc. 121 (1999) 9893.
[159] D. Lee, S.J. Lippard, 1999, unpublished results.
[160] T.J. Mizoguchi, S.J. Lippard, J. Am. Chem. Soc. 120 (1998) 11022.
[161] T.J. Mizoguchi, R. Davydov, S.J. Lippard, 1999, unpublished results.

[162] G. Roelfes, M. Lubben, K. Chen, R.Y.N. Ho, A. Meetsma, S. Genseberger, R.M. Hermant, R. Hage, S.K. Mandal, V.G. Young Jr, Y. Zang, H. Kooijman, A.L. Spek, L. Que Jr, B.L. Feringa, Inorg. Chem. 38 (1999) 1929.
[163] R.Y.N. Ho, G. Roelfes, R. Hermant, R. Hage, B.L. Feringa, L. Que Jr., Chem. Commun. (1999) 2161.
[164] R.Y.N. Ho, G. Roelfes, B.L. Feringa, L. Que Jr, J. Am. Chem. Soc. 121 (1999) 264.